ANODIC OXIDATION AND DEPTH DISTRIBUTION STUDIES

WITH

V, Mo, AND W

ANODIC OXIDATION AND DEPTH DISTRIBUTION STUDIES

WITH

V, Mo, AND W

By

MULK RAJ ARORA

A Thesis

Submitted to the Faculty of Graduate Studies

in Partial Fulfilment of the Requirements

for the Degree

Master of Science

McMaster University

March, 1971

MASTER OF SCIENCE (1971)
(Metallurgy and Materials Science)

McMASTER UNIVERSITY
Hamilton, Ontario

TITLE: Anodic Oxidation and Depth-Distribution Studies with V, Mo, and W.

AUTHOR: Mulk Raj Arora, B. Tech. (Indian Institute of Technology, Bombay)

SUPERVISOR: Professor R. Kelly

NUMBER OF PAGES: x, 85

SCOPE AND CONTENTS:

This investigation is primarily concerned with the development of a suitable high-precision sectioning technique to be employed in studies of depth distributions of energetic ions in Mo and V. It consists of two main parts.

In the first part, uniform anodic oxide films of controlled thicknesses have been grown on polycrystalline V, Mo, and W (the latter, primarily, for comparison with earlier works on W) in acetic acid-sodium tetraborate solutions containing small quantities of water. These anodic films, which show bright characteristic interference colours when formed at >10 volts, are shown to be rapidly soluble in a dilute solution of KOH whereas the underlying metal is attacked at a rate of less than $\sim$100Å

per day. The thickness of the anodic films per volt has been established using ellipsometry and conventional weight-loss measurements.

Kinetics of anodization have been studied at constant-current and constant-voltage. An analysis of these data shows the composition of the films on Mo and W to be close to MoO_3 and WO_3 respectively while those on V were intermediate between V_2O_4 and V_2O_5. The density of the films on Mo and the differential field strength, E_d, for films on Mo and W have also been determined.

In the second part, a theoretical background consisting of an outline of the theory of Lindhard, Scharff and Schiøtt, has been provided; in the absence of experimental data, this theory is generally used to estimate the depth distribution of ions in amorphous targets. Experimental range profiles have been determined for 5-30 keV Kr^{85} in polycrystalline Mo using the technique developed in the first part and the results obtained show a large discrepancy when compared with Lindhard theory. The extent of disagreement with theory is similar to that obtained by previous workers with targets such as Al or W.

Evidence is presented to show that this large discrepancy may be attributed to crystal-lattice effects (i.e. channelling). For example, it is shown that the discrpency is not due to the anodizing-stripping sequence being sensitive to bombardment. Also, it is demonstrated that the Mo used had a pronounced preferred orientation such that the open directions <100>, <211>, and <111> were normal to the surface.

An important part of future work will be to extend techniques such as those described here to the metal Be, for Be is the lightest target material that can be conveniently worked with.

Acknowledgements

The author gratefully acknowledges the interest, continuous guidance, and encouragement of Dr. R. Kelly throughout the course of this work.

The author also wishes to thank Dr. J. Shewchun, Mr. K.K. Gupta and Mr. Colin Rowe (now at Northern Electric Co., Ottawa) for their assistance in ellipsometry measurements.

This project was supported by grants from the Defense Research Board and National Research Council of Canada to Dr. R. Kelly and by the Ontario Government to the author.

TABLE OF CONTENTS

LIST OF ILLUSTRATIONS

LIST OF TABLES

CHAPTER 1

Introduction

A great deal of attention has been devoted in recent years to studying the interaction of energetic charged particles with matter. In particular, a knowledge of the depth of penetration of such particles injected into solid materials is of interest in interpreting radiation damage and sputtering phenomena, in preparing targets for nuclear research, and in fabricating solid-state semi-conductor devices. From a theoretical viewpoint, such an investigation is of fundamental interest in the estimation of screened-interaction potentials and in the elucidation of the mechanism of energy transfer in elastic and inelastic scattering of charged particles. However, in the energy range below 1 MeV, experimental data have been obtained on the depth of penetration of heavy ions only in a limited number of target materials.

The current lack of experimental data may largely be attributed to the difficulties encountered in trying to measure extremely small depths of penetration. The mean range of a 45 KeV Cs^{137} ion in aluminum, according to the Bohr-Nielsen theory (1), is about 5 $\mu g/cm^2$, or 785 Å. Obviously, for ions of such short range, it would be difficult if not impossible to prepare sufficiently thin foils for studying the depth of penetration by conventional stacked-foil techniques. To overcome such problems, Davies et al. (2) developed an extremely sensitive and reliable radiochemical sectioning technique, the so-called "peeling

method". It consisted of electrochemical oxidation of aluminum at constant voltage in aqueous ammonium citrate, followed by removal of the oxide film in a phosphoric acid - chromic acid solution. Due to the highly protective nature of the aluminum oxide film, this two-step process enabled very uniform surface layers of metal, as thin as 1 $\mu g/cm^2$ (i.e. 37 Å), to be removed. Since their pioneering work on aluminum, similar techniques have also been developed for tungsten, silicon and gold (3-22), and much work has accordingly been done in the region of mass 30 (Al, Si) and mass 190 (W, Au). This leaves a great deal of work to be done with extremely light targets, such as Be, and in the region between Si and W. For the present work, two metals, V (mass 51) and Mo (mass 96), were chosen in an attempt to extend the spectrum of masses from light to heavy ones. Since sufficiently sensitive and reliable sectioning techniques were not available, they had to be developed before the actual work on the depth-distribution studies could begin.

This thesis is, therefore, in two parts. The first part, Chapter 2, deals with the anodic oxidation of V and Mo, in which "peeling" methods are developed, calibrated, and compared with that previously established for W. The second part, Chapter 3, describes the preliminary use of these techniques in studying the depth distribution of Kr^{85} in Mo.

CHAPTER 2

Anodic Oxidation Studies with V, Mo, and W

2.1 Theory of Anodic Oxidation

The growth of anodic films is basically a problem in the ionic conductivity of oxides at high field strengths, complicated by the processes occurring at the metal/oxide and the oxide/electrolyte interfaces. Some of the classical theories are discussed below, all of them being based on an idealized, homogeneous, parallel-sided film which is free from flaws.

2.1.1 Verwey's Model

Verwey (23) made the following assumptions:

i) Metal ions at interstitial sites are the mobile entity (this is a highly artificial assumption, though is not critical since a similar equation is obtained for any other mobile point defect).

ii) All interstitial ions are equivalently placed as regards their ease of movement (this is only an approximation since there must be a range of site types, jump distances, and potential barriers due to the amorphous nature of most anodic oxides).

iii) No interstitial blocks the path of another.

iv) Concentration of the mobile species has value corresponding to electroneutrality (i.e., value in the bulk oxide).

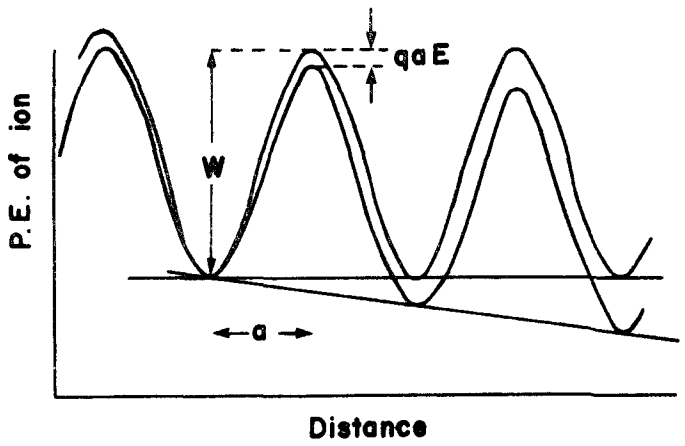

Fig. 1 Potential Energy (P.E.) of mobile ions vs. distance with and without field.

The governing equation is derived by picturing the ions as acquiring sufficient energy from thermal agitation plus the applied field to jump the potential energy barrier, as shown in Figure 1, and thus reach the next site.

In the absence of an electric field, the number of ions jumping in any direction is given, in units of ions/cm^2-sec, by

$$i = 2an\nu \exp\left[-\left(\frac{W}{kT}\right)\right]$$

where a = activation distance, equivalent to half-jump distance

ν = frequency of vibration of interstitial ion, including a factor of the type $\exp\left(\frac{\Delta S}{R}\right)$

n = number of mobile ions per unit volume

In the presence of an electric field, the flux of mobile ions will be greater in the direction of the field, due to the lower potential barrier, as compared to the flux against the field. This will result in a net flux of ions in the direction of the applied field. Expressing current in terms of ions/cm^2-sec., we have for the observed current

$$i = \vec{i} - \overleftarrow{i}$$

where

$$\vec{i} = 2an\nu \exp[-(\frac{W-qaE}{kT})] \qquad (1)$$

$$\overleftarrow{i} = 2a\{n + 2a(\frac{\partial n}{\partial x})\}\nu \exp[-(\frac{W + qaE}{kT})];$$

$\frac{\partial n}{\partial x}$ = concentration gradient of the mobile ions;

q = charge of each ion.

Then

$$i = \vec{i} - \overleftarrow{i}$$

$$= 4an\nu \exp[-(\frac{W}{kT})]\text{Sinh}(\frac{qaE}{kT}) - 4a^2\nu\frac{\partial n}{\partial x} \exp[-(\frac{W + qaE}{kT})] \qquad (2)$$

Substitute $A = 2an\nu\exp[-(\frac{W}{kT})]$; $B = \frac{qa}{kT}$ in equation 2 to get

$i = 2A\text{Sinh}BE$ - diffusion term

At very low fields, i.e., for $\frac{qaE}{kT} << 1$

For $qaE/kT << 1$, we have

$$\text{Sinh}\frac{qaE}{kT} \simeq \frac{qaE}{kT} \; ; \quad \frac{W + qaE}{kT} \simeq \frac{W}{kT}$$

and therefore

$$i \simeq \text{Constant}.E - \text{Constant}.\frac{\partial n}{\partial x}$$

$$= \sigma E - D_o\frac{\partial n}{\partial x} \qquad (3A)$$

where σ = Ohm's law conductivity

D_o = diffusivity as per Fick's first law.

At very high fields, i.e., for $\frac{qaE}{kT} >> 1$

At the other extreme, we have qaE/kT >> 1, so that $\vec{i}$ becomes much greater than $\overleftarrow{i}$, to the order of 10^{10} times, and so

$$i \simeq \vec{i}$$

$$= A \exp BE \tag{3B}$$

It is of interest to examine the Verwey model numerically and determine whether one of 3A or 3B is always valid under anodic oxidation conditions. Rewriting equation 2, we have for the general expression for ionic current,

$$i = 4a\nu \exp[-(\frac{W}{kT})]\{n\mathrm{Sinh}[\frac{qaE}{kT}] - a \exp[-(\frac{qaE}{kT})]\frac{\partial n}{\partial x}\}$$

$$= C\{n \mathrm{Sinh}[\frac{qaE}{kT}] - a \exp[-(\frac{qaE}{kT})]\frac{\partial n}{\partial x}\}$$

where $C = 4a\nu \exp[-(\frac{W}{kT})]$; two terms will be recognized:

$$\text{field-assisted term} = C \cdot n\mathrm{Sinh}[\frac{qaE}{kT}] \tag{4}$$

$$\text{diffusion term} = C \cdot a \exp[-(\frac{qaE}{kT})]\frac{\partial n}{\partial x} \tag{5}$$

To maximize the diffusional term, we assume that there is the maximum possible concentration gradient, i.e.,

$n = n$ at $x = 0$ (at the metal/oxide interface)

$= 0$ at $x = 2a$ (one atom layer away)

Then, $a\frac{\partial n}{\partial x} = \frac{n}{2}$

and the relative contribution to the current due to the field-assisted and diffusional terms is given by

$$\frac{\text{Field-assisted term}}{\text{Diffusion term}} = \frac{2\ \text{Sinh}(\frac{qaE}{kT})}{\exp[-(\frac{qaE}{kT})]}$$

Under typical operative conditions of anodic oxidation, we can assume values for the various parameters as follows:

$E \geq 3 \times 10^6$ volts/cm

$a \simeq 1.5°A$

$q = 2$ if oxygen mobile

> 2 if cation or both species mobile

$kT = \frac{1}{40}$ eV at room temperature

The estimate for E is based on the common observation that anodic oxide films have a thickness which is less than $\sim 35°A/$ volt. Then

$$\frac{\text{Field-assisted term}}{\text{Diffusion term}} \simeq \frac{2\text{Sinh}(3.6)}{\exp(-3.6)} \simeq 1360$$

i.e., field-assisted migration always dominates over the diffusional term due to concentration gradient and hence the ionic current according to Verwey's model will always be the same as for high field, i.e.,

$$i = A\ \exp BE \qquad (3)$$

This point has not been fully appreciated in previous work (e.g. 23)

2.1.2 Mott and Cabrera's Model (24-25)

This model takes into consideration the surface space charge at the metal-oxide interface. The field-strength in the oxide will change, according to Poisson's equation, only if volume space charge is present and this change is given, in e.s. units, by

$$\frac{\partial E}{\partial x} = \frac{4\pi\rho}{\varepsilon}$$

where ρ = volume space charge density

ε = dielectric constant

The net volume space charge is due to the inequality between the positive space charge due to the mobile ions and the negative space charge due to the conjugate non-mobile species (electronic space charge would tend to be swept away at such high fields).

If the volume space charge density is not too great, then the change in field across the oxide, a function of the total charge present in the oxide, must be small for a thin enough film, i.e., the field in the oxide film is a constant to a first approximation. Moreover, the current will then be controlled only by the rate of entry of ions into the oxide provided, as assumed by Mott and Cabrera, that the first

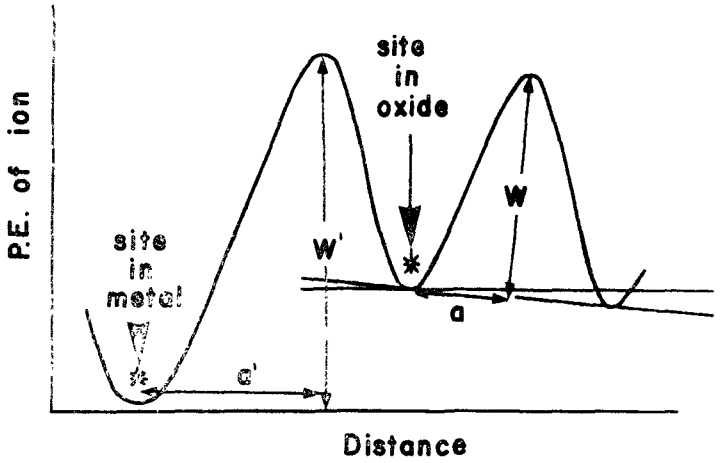

Fig. 2

Potential Energy vs. distance for ion entering oxide from the metal, with applied field.

barrier to be surpassed by ions entering the oxide is sufficiently higher than later barriers, as shown in figure 2.

The current across the entrance barrier is given by

$$i = n'\nu' \exp\left[-\left(\frac{W'-qa'E}{KT}\right)\right] \qquad (6A)$$

where n' = concentration of ions per cm^2 at the interface and primes are used to identify parameters associated with the entrance barrier.

The concentration, n, of ions within the oxide is not fixed; it adjusts itself (in the steady state) until the current within the oxide, assuming high-fields, namely

$$i = 2an\nu \exp[-(\frac{W-qaE}{kT})] \tag{6B}$$

just equals that across the entrance barrier, i.e.,

equation 6A = equation 6B

This gives $n = n_o$, where

$$n_o = \frac{(n'\nu')^{a/a'}}{2a\nu} \exp[\frac{W - \frac{aW'}{a'}}{kT}] \; i^{(1-\frac{a}{a'})} \tag{7}$$

The question as to whether this model could be ever expected in practice will be considered in connection with the following model.

2.1.3 Young's Model (26)

This is a general treatment with the above two models as the limiting cases.

Assume that the concentration of mobile metal ions in the electrically neutral oxide is p. The space charge due to the conjugate non-mobile species is thus (-pq) where q is the charge on metal ions. Then, Poisson's equation gives

$$\frac{\partial E}{\partial x} = \frac{4\pi q}{\varepsilon} (n-p)$$

where (n-p) is the number of mobile ions in excess to those required for electrical neutrality and n = n(x) is as before the actual concentration of mobile metal ions in the oxide during anodization.

The current at point x in the oxide is

$$i = 2an\nu \exp[-(\frac{W}{kT})] \exp[\frac{qaE}{kT}] \tag{8}$$

Under steady-state conditions, it follows that $i \neq i(x)$; however, we must anticipate that both n and E vary with x. Writing $B = \frac{qa}{kT}$,

$$\frac{\partial i}{\partial x} \alpha \left(\frac{\partial n}{\partial x} + nB\frac{\partial E}{\partial x}\right) = 0$$

Substituting for $\frac{\partial E}{\partial x}$ from Poisson's equation yields

$$\frac{\partial n}{\partial x} + nB\frac{4\pi q}{\epsilon}(n - p) = 0$$

Integrating, we get

$$n(x) = p\left[1 - \left(1-\frac{p}{n_o}\right) \exp\left(-\frac{4\pi qpBx}{\epsilon}\right)\right]^{-1}$$

where n_o is the value of n(x) at x=0, given by equation 7. Substituting for n(x) in equation 8, we get

$$E(x) = E_o + \frac{1}{B} \log\{p^{-1}[n_o-(n_o-p) \exp(-\frac{4\pi qpBx}{\epsilon})]\} \qquad (9)$$

where E_o, equal to $\frac{W}{qa} + \frac{1}{B} \log\frac{i}{2an_o\nu}$, is the value of E(x) at x=0 and given by equation 6A. n(x) and E(x) are thus both determined.

Equation 9 reduces to Mott's relation (i.e., $E = E_o$) for small x and to Verwey's relation for large x (i.e., $E = \frac{W}{qa} + \frac{1}{B}\log\frac{i}{2ap\nu}$). The field thus changes with thickness at first but eventually becomes constant at Verwey's value.

It might be suspected that the physical limitation that a film cannot be less than one unit cell thick may mean that the film may never be thin enough for Mott's model to be applicable. We have confirmed this by assuming values for the various parameters as follows:

$q = 2$ $\qquad\qquad$ $\epsilon = 10$

$p = 10^{14}$ ions/cm^3 $\qquad$ $x = 30 \times 10^{-8}$ cm

$a = 1.5$°A

Then, $\frac{4\pi qpBx}{\varepsilon} \simeq 27{,}000$

and $\exp(-\frac{4\pi qpBx}{\varepsilon})$ becomes extremely small to give Verwey's value for the field. Since the values assumed for various parameters are all conservative, it may be said that Mott's case never holds in practice. For example, a value of 10^{14} ions/cm^3 for p corresponds to an impurity content of 10^{-8} atom fraction, which is inconceivably low for an oxide.

2.1.4 Field Production of Frenkel Defects in Steady State.

This model was proposed separately by Bean, Fisher and Vermilyea in 1956 (28) and by Dewald in 1957 (29).

At high field strengths, ions may be pulled out of lattice positions into interstitial positions, creating Frenkel defects. This model assumes that the vacant cation sites are immobile and that only the interstitial ions move (rather an artificial assumption since if field is strong enough to create a Frenkel defect, it should be more than enough to move a lattice ion into an adjacent empty site, i.e., ΔE for lattice site → interstitial is greater than ΔE for lattice site → next lattice site). The essential features of this model are that p now becomes field-dependent and that n=p at all times, i.e., the oxide is always electrically neutral.

The rate of production of Frenkel defects and hence of vacant cation sites, which contribute to p, is assumed to be

$$(N_o - m)\nu_1 \exp[-(\frac{W_1 - qa_1E}{kT})]$$

where N_o = concentration of lattice sites

m = concentration of Frenkel defects

Subscript 1 refers to the process lattice ions → interstitial ions. Subscript 2 refers to the mobility of interstitial ions.

The vacant sites are filled by their capturing interstitial ions moving through the oxide. Assume that rate of filling is given by (flux of ions)(concentration of vacant sites)(cross-section of vacant lattice sites) = $im\sigma$. Then,

$$\frac{\partial m}{\partial t} = (N_o - m)\nu_1 \exp[-(\frac{W_1 - qa_1E}{kT})] - i\sigma m$$

The further important assumption is now made that m = p, i.e., there is no source of immobile space charge other than vacant cation sites, whence n = m, where n is as usual the total concentration of mobile metal ions. Then,

$$i = 2a_2 m\nu_2 \exp[-(\frac{W_2 - qa_2E}{kT})]$$

In the steady state, $\frac{\partial m}{\partial t} = 0$, and for $N_o >> m$, we get,

$$m = (\frac{\nu_1 N_o}{2\sigma a_2 \nu_2})^{1/2} \exp[-(\frac{W_1 - W_2}{2kT})] \exp[\frac{q(a_1 - a_2)}{2kT} E]$$

$$i = 2a_2\nu_2(\frac{\nu_1 N_o}{2\sigma a_2 \nu_2})^{1/2} \exp[-(\frac{W_1 + W_2}{2kT})] \exp[\frac{q(a_1 + a_2)}{2kT} E]$$

$$= A' \exp B'E \qquad (10)$$

where A' and B' are the appropriate parameters.

2.1.5 Generalized Model

Writing down the expressions for ionic current thus far discussed, we have:

Verwey's model: $i = 2an\nu \exp[-(\frac{W-qaE}{kT})]$ equation 1

$= 2an\nu \exp(-\frac{W}{kT}) \exp(\frac{qaE}{kT})$

$= A \exp BE$

Mott and Cabrera's Model: $i = n'\nu' \exp[-(\frac{W'-qa'E}{kT})]$ equation 6A

$= A \exp BE$

Young's model: $i = 2an\nu \exp[-\frac{W}{kT}] \exp(\frac{qaE}{kT})$ equation 8

$= A \exp BE$

Bean et al's model $i = 2a_2\nu_2(\frac{\nu_1 N_o}{2\dot{\sigma}a_2\nu_2})^{1/2} \exp[-(\frac{W_1+W_2}{2kT})] \exp[$

$\frac{q(a_1+a_2)}{2kT} E]$ equation 10

$= A \exp BE$

We note that all these models result in the same form for the relation between i, E and T, i.e.,

$$i = A \exp BE$$

Hence, the experimental data are independent of the model for the particular models discussed and should give a simple voltage vs. time behaviour at constant current. This in turn means that there is no valid experimental distinction between the models though this conclusion does not exclude other models (e.g. one where there is a range of 'a' or 'W' values) from being important.

2.1.6 Consequences of the Amorphousness of the Anodic Oxide

Ions moving through the film will encounter not a series of

identical barriers but a series of barriers with a range of activation distances 'a' and heights 'W'. Assuming a gaussian distribution for them, Young (30) found that the Tafel slope, $\frac{\partial E}{\partial \ln i} = \frac{kT}{qa}$, increases with field instead of remaining constant. This is a conclusion of particular importance in view of the demonstrated lack of difference between the earlier models.

2.1.7 Certain Inadequacies of the Above Models

i) All the above models predict for the steady-state current

$$i = i_o \exp(-\frac{W}{kT}) \exp(\frac{qaE}{kT})$$

This relation leads to the conclusion that the Tafel slope, $\frac{\partial E}{\partial \ln i}$, is independent of E at a given T and proportional to T. Vermilyea (31), however, found that in the case of Ta, the Tafel slope was independent of T. Later experiments of Young (30) were fitted by replacing $(W-qaE)$ by $(W-|\alpha|E + |\beta|E^2)$.

Vermilyea (32) also carried out transient experiments. He changed the field rapidly from a given initial value, under which steady-state conditions had been set up, and observed the immediate value of the ionic current at the new field. He assumed that in this case the change in current was due solely to a change in the mean velocity of whatever mobile species are present, no change occurring in their concentration. He found that under these conditions the relation $(\frac{\partial E}{\partial \ln i})_{transient} \propto T$, which is expected from the above models, was not observed, this slope actually decreasing with increasing temperature under the conditions used. Later measurements by Young (33) could, once again, be described by the substitution $W(E) = W_o - |\alpha|E + |\beta|E^2$ in the

equation for ion mobility. This implies that the Tafel slope depends on E at constant T. This substitution is based on a Schottky-type law in which the ions move freely along channels in the oxide except where they become trapped by Coulombic attraction for local excess negative charge. Due consideration of the amorphous nature of anodic oxides also tends to fit the data better.

ii) In all the above models, it was assumed that only the metal ions are mobile. However, the tracer work of Davies et al (34) indicates that with Ta, Nb, Al, W, both ions are not only mobile, but the metal and oxygen ions also travel right through the film. This observation that both ions are mobile during the ordinary growth process to comparable extents over a wide range of currents presents considerable difficulties to these models. The chief one is that any model with independent metal and oxygen ion currents would be expected to display a rapid change with field in the ratio of the two currents unless one had a fortuitously close similarity between values of activation energies and activation distances, which is quite unlikely to occur with more than one metal.

2.2 Structure of Anodic Films

The structure of anodic oxide films on Mo, V and W may be described as glassy or amorphous (35, 36), hence with short-range order. The normal oxides on Mo and W are found to have structures intermediate between the types ReO_3 and TiO_2 (rutile)(Fig. 3). ReO_3 has a structure in which MO_6 octahedra are joined by sharing corners. The rutile structure also consists of MO_6 octahedra but these are linked by sharing

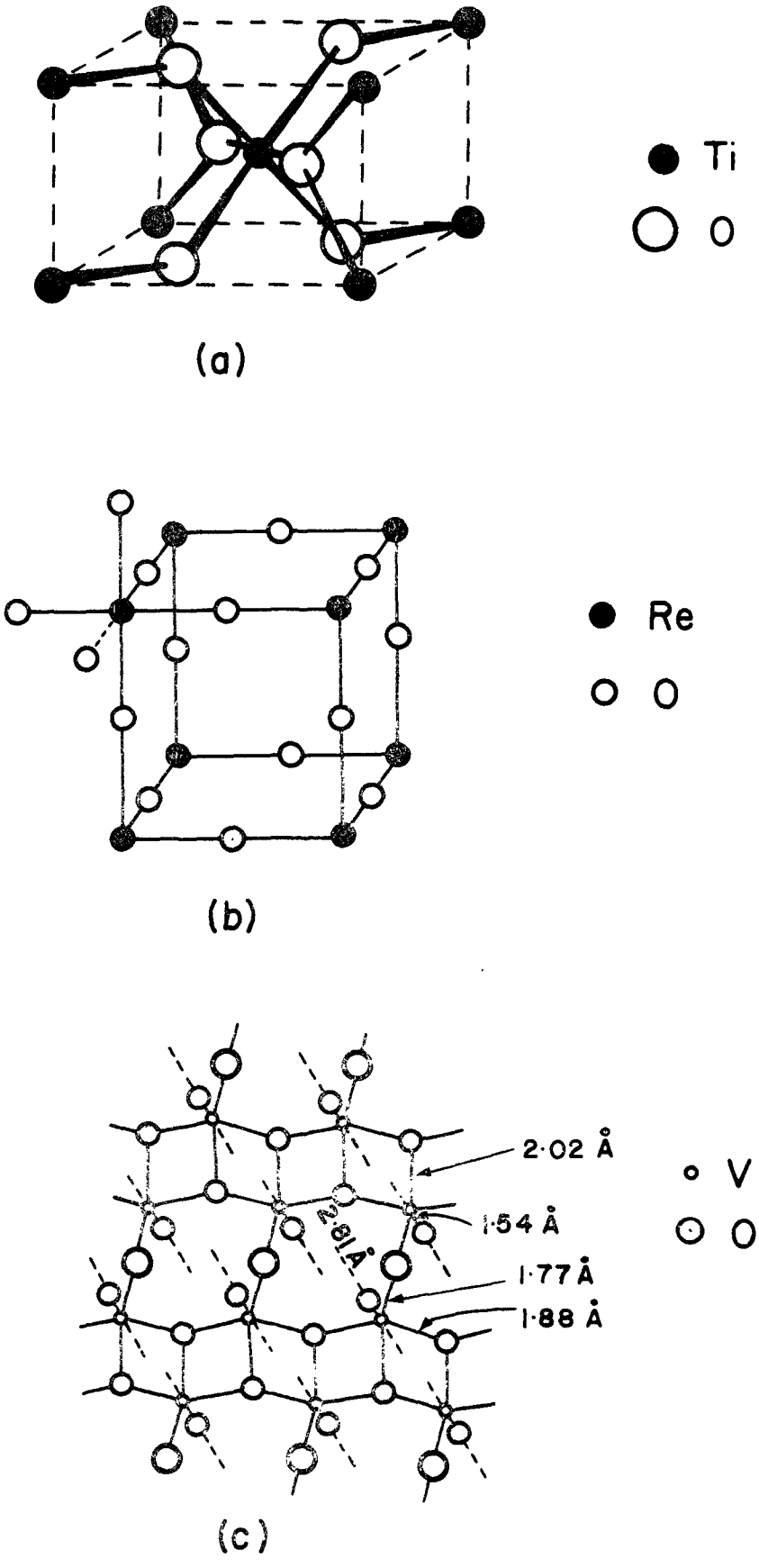

Fig. 3 a)Rutile Structure, TiO_2 b) ReO_3 Structure c) V_2O_5 Structure

edges to give extended chains. In between these two extremes, a whole series of structures can be envisaged, of stoichiometry M_nO_{3n-1}, in which oxygen is progressively economized by allowing slabs of corner-linked octahedra to be joined to identical slabs by edge-sharing; the smaller the n, the greater the economy of oxygen.

The lower oxides on V show similar behaviour of having intermediate shear phases, but in this case the rutile structure is the parent phase and the general formula is M_nO_{2n-1}. The geometrical basis for the sequence is the increasing face-sharing of oxygen between MO_6 octahedra rather than the edge- and corner-sharing.

The pentavalent V has a structure quite different from those of lower oxides; in this case, the V atoms have a rather irregular type of 5-coordination; there are chains formed of tetrahedral groups linked through corners and these chains are so placed together that each V has a fifth O neighbour in the other chain (Fig. 3c). The bond lengths in V_2O_5 for various oxygen sites are 1.54 Å, 1.77 Å, 1.88 Å (2 atoms), 2.02 Å; the next nearest O neighbour of V in V_2O_5 is in the adjacent layer at a distance of 2.81 Å, and with other five, this completes a very distorted octahedron.

2.3 Ellipsometry

Ellipsometry (37) is the measurement of the effect of reflection on the state of polarization of light. It can be used to yield the optical constants of the reflecting materials, or when the reflecting material is a film-covered substrate, both the thickness and the optical constants of the film. The main advantage of ellipsometry is its applicability to strongly absorbing media. The refractive index, n, the

extinction coefficient for the absorbing media, and the thickness of the film can be determined over the whole range of thickness from the monoatomic to microns.

2.3.1 General Principles

Ellipsometry is concerned with reflection of monochromatic, collimated, polarized light. The state of polarization is completely defined by the amplitude and phase relationships between the 'p' (parallel to the plane of incidence) and 's' (perpendicular, "senkrecht", to the plane of incidence) components of the electric field oscillations. If 'p' and 's' are in phase (i.e., have phase difference of $m\pi$), then the resultant wave is said to be plane-polarized; otherwise, it corresponds to elliptical polarization. In general, reflection causes a change in the relative phases of the 'p' and 's' waves and a change in the ratio of their amplitudes. The effect of reflection is therefore characterized by the angle Δ, defined as the change in phase, and the angle ψ, the arctangent of the factor by which the amplitude ratio changes. Symbolically, if the amplitudes of the incident and reflected beams are designated E and R, respectively, and the phase angles β, then

$$\Delta = (\beta_p - \beta_s)_{reflected} - (\beta_p - \beta_s)_{incident} \tag{11}$$

$$\psi = \arctan \left(\frac{R_p}{R_s} \cdot \frac{E_s}{E_p}\right) \tag{12}$$

Ellipsometry is the measurement of Δ and ψ.

2.3.2 Measuring Procedure

The incident monochromatic beam is transmitted through the sequence of a collimator, a polarizer, and a quarter-wave plate. The

azimuthal orientations of these devices determine the relative amplitudes and phase differences between the 'p' and 's' components of the incident beam. These orientations are adjusted so that the difference in phase of incident beam just compensates that which results from reflection, giving rise to a plane-polarized reflected beam. Δ is thus measured.

The plane-polarized reflected beam is then transmitted by the analyzer to a telescope and a detector. Provided the polarizer and the compensator are oriented as described above, the analyzer can be oriented to extinguish the reflected beam. This extinction setting thus measures ψ.

The actual procedure consists of fixing the orientation of the quarter-wave plate so that the fast axis is inclined at 45° to the plane of incidence. With the fast axis thus oriented, the relative phases and amplitudes of the 'p' and 's' components of the beam transmitted by the quarter-wave plate depend just upon the orientation of the polarizer, and any phase difference, 0° to 360°, can be achieved. This dependence has been derived by Archer et al (38) and Winterbottom (39), as given below.

The measuring procedure consists of adjusting the polarizer and analyzer so that the detected beam is extinguished. Such extinction is not a sharp point and hence its determination requires an iterative process. Both the polarizer and the analyzer are adjusted as close to extinction as possible by trial and error; then, keeping the polarizer setting fixed, the position of the analyzer is varied and 2-3 pairs of observations are taken on both sides of extinction. The analyzer is then fixed at their average and the position of the polarizer is next changed, again to take 2-3 paired observations on both sides of the maximum

extinction. Next step is to fix the polarizer at the average of the last observations and the process repeated with the analyzer once again. This iterative process of fixing the analyzer or the polarizer at its last observed average and adjusting the other is repeated till self-consistent angles for both are obtained. Generally it takes 2-3 iterations with each to get the desired results, i.e., with an uncertainty in Δ and ψ of $\pm 0.02°$.

There are two orientations of the polarizer which lead to plane-polarized, extinguishable reflected light, namely,

$$\Delta' = -\Delta$$

and

$$\Delta' = -\Delta + 180°$$

Designating the former of these extinction settings as P_o and the latter P_o' and following the treatment of Archer (38) and Winterbottom (39) for a quarter-wave plate compensator, we get

$$P_o' = P_o \pm 90°$$

$$\Delta = 90° - 2P_o = 270° - 2P_o'$$

$$\psi = -A_o = A_o'$$

There might thus appear to be an ambiguity as to the value of Δ. But ψ can vary only between 0 and 90°; from this fact the sign of the analyzer extinction setting determines whether the setting corresponds to the "primed" or "unprimed" case.

2.3.3 Interpretation of Ellipsometric Measurements

The relationship between Δ and ψ and the properties of a reflecting system are expressed by the Fresnel reflection coefficients. The

Fresnel reflection coefficient, r, of an interface is the ratio of the electric field vector, $\hat{R}$, of the reflected wave to that, $\hat{E}$, of the incident wave; in terms of the amplitudes of the incident and reflected waves E and R, respectively, and the phase change, β, accompanying reflection, we thus have,

$$r = \frac{R}{E} e^{i\beta} \tag{13}$$

The coefficient depends upon the orientation of the wave relative to the plane of incidence, and the reflection of a wave of any polarization is described by the two coefficients, r_s and r_p, for the component waves. The ratio of the reflection coefficients is

$$\frac{r_p}{r_s} = \left(\frac{R_p}{R_s} \cdot \frac{E_s}{E_p} \right) e^{i(\beta_p - \beta_s)} \tag{14}$$

$$= \tan \psi \cdot e^{i\Delta} \tag{15}$$

The above equations relate ψ and Δ to r_p/r_s. Finally, to complete the argument, we must introduce the indices of refraction. For an optically isotropic substrate with a clean surface the Fresnel reflection coefficients are

$$r_{12}^p = \frac{n_1 \cos\phi_2 - n_2 \cos\phi_1}{n_1 \cos\phi_2 + n_2 \cos\phi_1}$$

$$r_{12}^s = \frac{n_1 \cos\phi_1 - n_2 \cos\phi_2}{n_1 \cos\phi_1 + n_2 \cos\phi_2}$$

where ϕ_1 is the angle of incidence and ϕ_2 the angle of refraction and subscripts 1 and 2 refer to the surroundings and the substrate respectively. For an optically absorbing medium, the complex index of refraction of the substrate

$$\underline{n} = n - ik$$

is substituted for n_2 in the above equations and the value of n and k may be derived therefrom with a minimum of two independent measurements of ψ and Δ.

In case of reflection from a film covered substrate, the corresponding expression is

$$\tan\psi\, e^{i\Delta} = \frac{r_{12}^p r_{23}^p e^{-2i\delta}}{1+r_{12}^p r_{23}^p e^{-2i\delta}} \cdot \frac{1 + r_{12}^s r_{23}^s e^{-2i\delta}}{r_{12}^s r_{23}^s e^{-2i\delta}} \qquad (16)$$

where subscripts 1, 2 and 3 refer to the surroundings, film, and substrate respectively. Here, the number of independent measurements needed is so great that one normally assumes prior knowledge of the substrate constants; in the present case of Mo, the substrate constant was assumed to be 3.14 - i3.60*.

In equation 16, the real and the imaginary parts may be separated to yield equations for Δ and ψ; these are then plotted using a computer for given values of the angle of incidence, vacuum wavelength of light, and optical constants of the film and the substrate, plots for different optical constants being unique. Thickness in the plots is given in terms of δ, the relation being

$$\delta = \frac{360}{\lambda} d(n_1^2 - \sin^2\phi)^{1/2} \quad \text{degrees} \qquad (17)$$

$$d = \text{film thickness in } \mathring{A}$$

A typical plot is shown in Fig. 4. In practice, Δ and ψ are determined from experiments and compared with the computed plots to obtain the actual $\underline{n}$ and the thickness of the film.

* Private Communication from Mr. Colin Rowe (McMaster University)

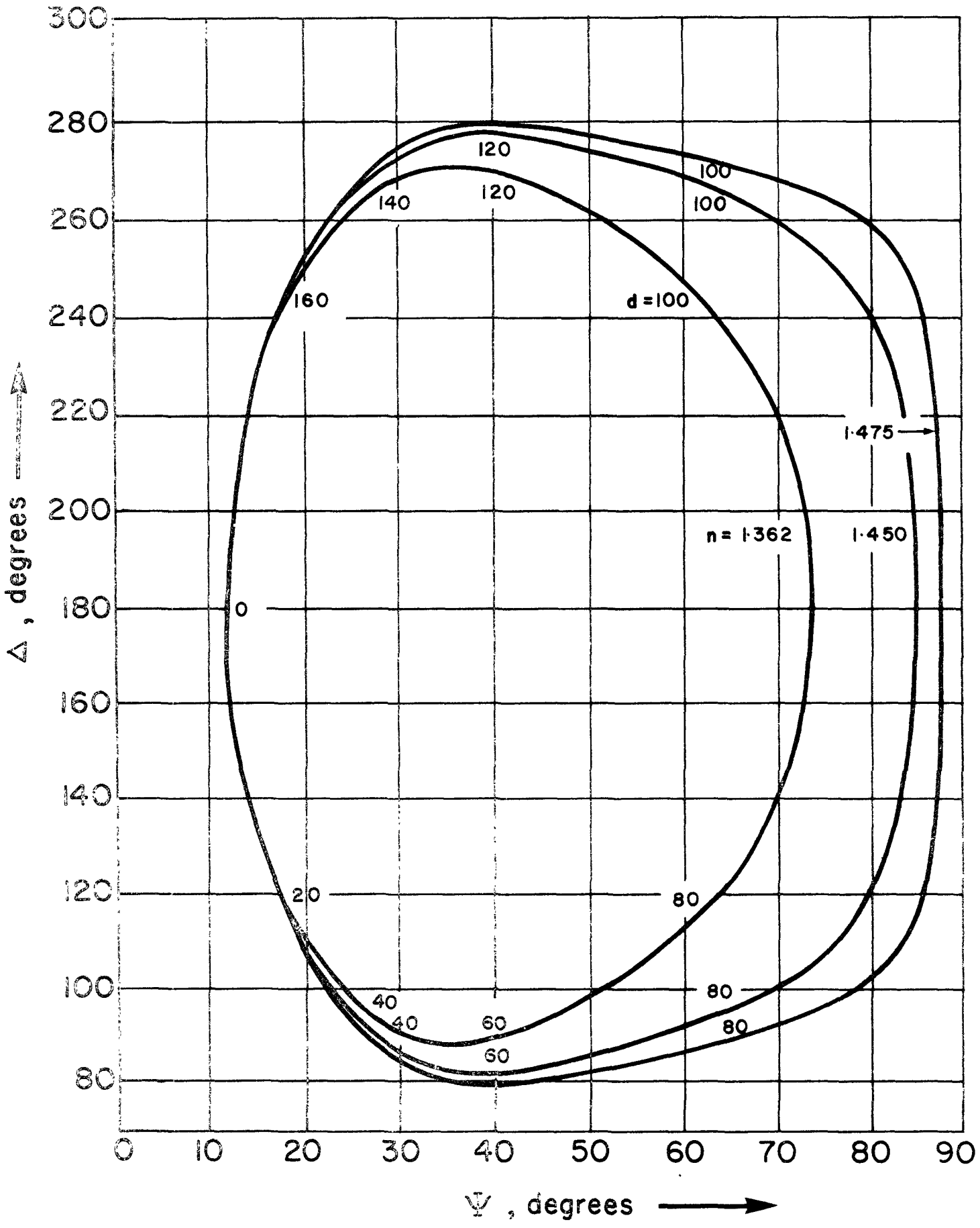

Fig. 4 Plot of Ellipsometric parameters, Δ vs. ψ

2.4 Anodizing Procedure

2.4.1 Materials

High-purity polycrystalline foils, 0.1 mm thick, were used as specimens throughout the work. They were degreased using petroleum ether, rinsed with distilled water, etched in dilute nitric acid and again rinsed with distilled water; they were then anodized at 80-100 volts several times and the anodic oxide films thus formed were dissolved in dilute potassium hydroxide solution (to be discussed later). This preanodizing treatment may be assumed to reduce the effective surface area of the foils (2), presumably by removing submicroscopic irregularities, and give a reproducibly flat clean surface of constant area. It is thus analogous to electropolishing but more controlled.

2.4.2 Anodizing Step

It has been shown in previous work (4) that W can be anodized in an aqueous solution of potassium nitrate (0.4M) and nitric acid (0.04M) at room temperature. Mo has not been successfully anodized before whereas V can apparently be anodized up to high voltages in electrolytes based on acetic acid (40). It was found in the present work, however, that anodic films on V, formed as in reference 40, were unstable in the atmosphere and so would not be of great use in experiments such as studying the depth-distributions of energetic ions in V.

Two electrolytes were finally selected and used throughout this work, both containing acetic acid and 0.02M sodium borate, but with water contents of 1.0 and 2.0M respectively. (The latter electrolyte,

with 2.0 M water, is that of Keil et al (40)). Higher amounts of water (>2.0 M) resulted in excessive dissolution of the films on V and Mo during anodizing, with the films also being rather difficult to stabilize. Specifically, with 5.0 M water in the electrolyte, fresh films tended to become non-uniformly thinner in 20 seconds (for V) or 25 seconds (for Mo) when exposed to the surrounding air; even when dried using compressed air immediately after formation, they were then found to be non-uniform and became even more so with time. Films formed in 1.0 M water electrolyte were not affected up to 45-50 seconds (in the absence of compressed air drying) and were found to be particularly stable when dried with compressed air immediately after formation. They could then be preserved in air for more than 1 day and in a desiccater for more than 2 weeks. Films formed in 2.0 M water electrolyte showed an intermediate behavior, being closer to that of 1.0 M electrolyte. Water contents of less than 1.0 M resulted in non-uniform anodic films, presumably due to the low conductivity of the electrolyte (cf. 41) These conclusions are all based on the observation of interference colours.

All the experiments were carried out at 25±1°C. Due to the hygroscopic nature of acetic acid, the conductivity of the electrolyte changes with time due to its exposure to the atmosphere. This change in conductivity became significant, however, only after eight to ten anodizings; therefore, the electrolytes were discarded after every six anodizings. A planar platinum foil acted as cathode. A calomel reference electrode was occasionally inserted into the bath during anodizing to measure the true voltage drop across the oxide film on the anode. However, except at the start of a run, this voltage was similar to the total

applied voltage; in general, the anodic voltage was therefore assumed to be identical with the total applied voltage.

All the specimens were anodized for six minutes, by which time the current had dropped to an almost limiting value of 0.1-0.4 ma/cm^2.

2.5 Results

2.5.1 General

Newly grown films on V and Mo were found to dissolve readily in distilled water and were also, as stated in section 2.4.2, unstable when kept in the atmosphere. However, by drying these films with compressed air, they became quite stable, i.e., there was no change in the uniformity of their interference colours for up to one day in the laboratory air, and only a slow rate of dissolution in distilled water. All the films on V and Mo were, therefore, stabilized by drying them with compressed air immediately after anodizing and the specimens were then placed in a desiccator. Similar difficulties did not arise with W and no such precautions had to be taken.

Above 10-15 volts, the presence of the oxide films on the anodized specimens could be detected visually and their uniformity verified by means of the characteristic interference colours that occur.

2.5.2 Calibration of Method

For thick films formed at ≥ 10 volts, the relation between the oxide film thickness and the anodic formation voltage was determined by the conventional weight-loss method. The specimens used were large enough to get meaningful weight-loss measurements, a minimum of 100 μg

being considered a reasonable weight difference. For thin films, formed at < 10 volts, ellipsometry was used to get the film thickness. All specimens were anodized at a current density of 2.0 ma/cm^2 till the desired voltage was reached and then the current was allowed to drop; total time of anodizing in each case was six minutes. Results of the calibration are shown in Figures 5 - 7 and analytical expressions for thickness per volt are given in Table I.

TABLE I

Water Content of Electrolyte	THICKNESS OF OXIDE FILM μg/cm^2		
	V*	Mo	W
1.0 M	? + 1.10 volts	1.40+1.61 volts	3.0 + 1.85 volts up to 15 volts; 10.0 + 1.40 volts above 15 volts
2.0 M	? + 1.38 volts	1.40+1.78 volts	3.0 + 1.92 volts up to 15 volts; 10.0 + 1.40 volts above 15 volts

In order to study the depth of penetration of radioactive ions in metals, it is necessary to know the total amount of metal removed in the anodizing plus stripping operation. The above experiments give only the amount of metal that is removed during the stripping process alone, i.e.,

* The intercept, which relates in part to the natural oxide, is still not established with V. The problem is that ellipsometry could not be used here due to lack of knowledge of the substrate constants.

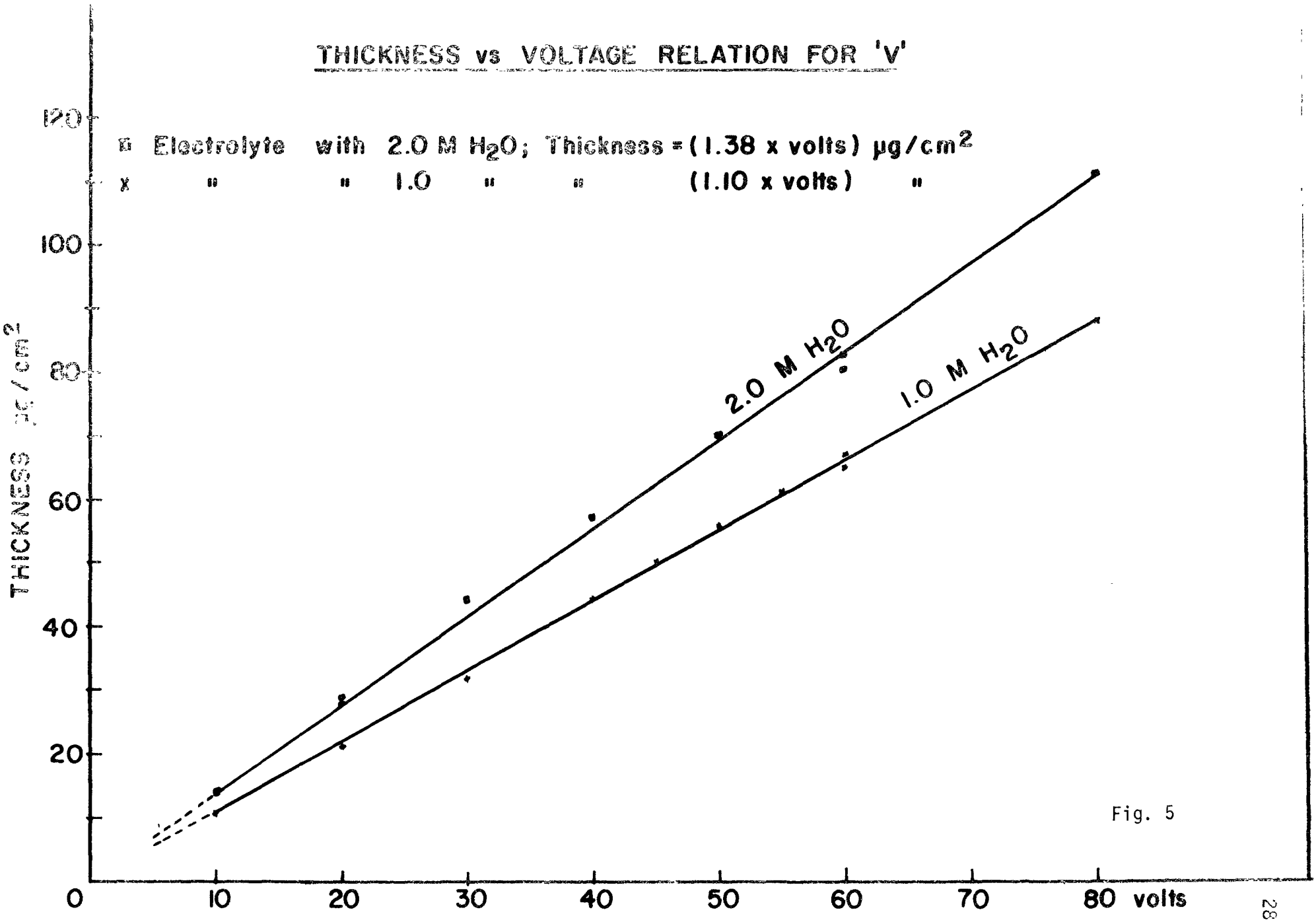
THICKNESS vs VOLTAGE RELATION FOR 'V'
□ Electrolyte with 2.0 M H_2O; Thickness = (1.38 x volts) µg/cm²
x " " 1.0 " " (1.10 x volts) "
THICKNESS µg / cm²
120
100
80
60
40
20
0
10
20
30
40
50
60
70
80 volts
2.0 M H_2O
1.0 M H_2O

Fig. 5

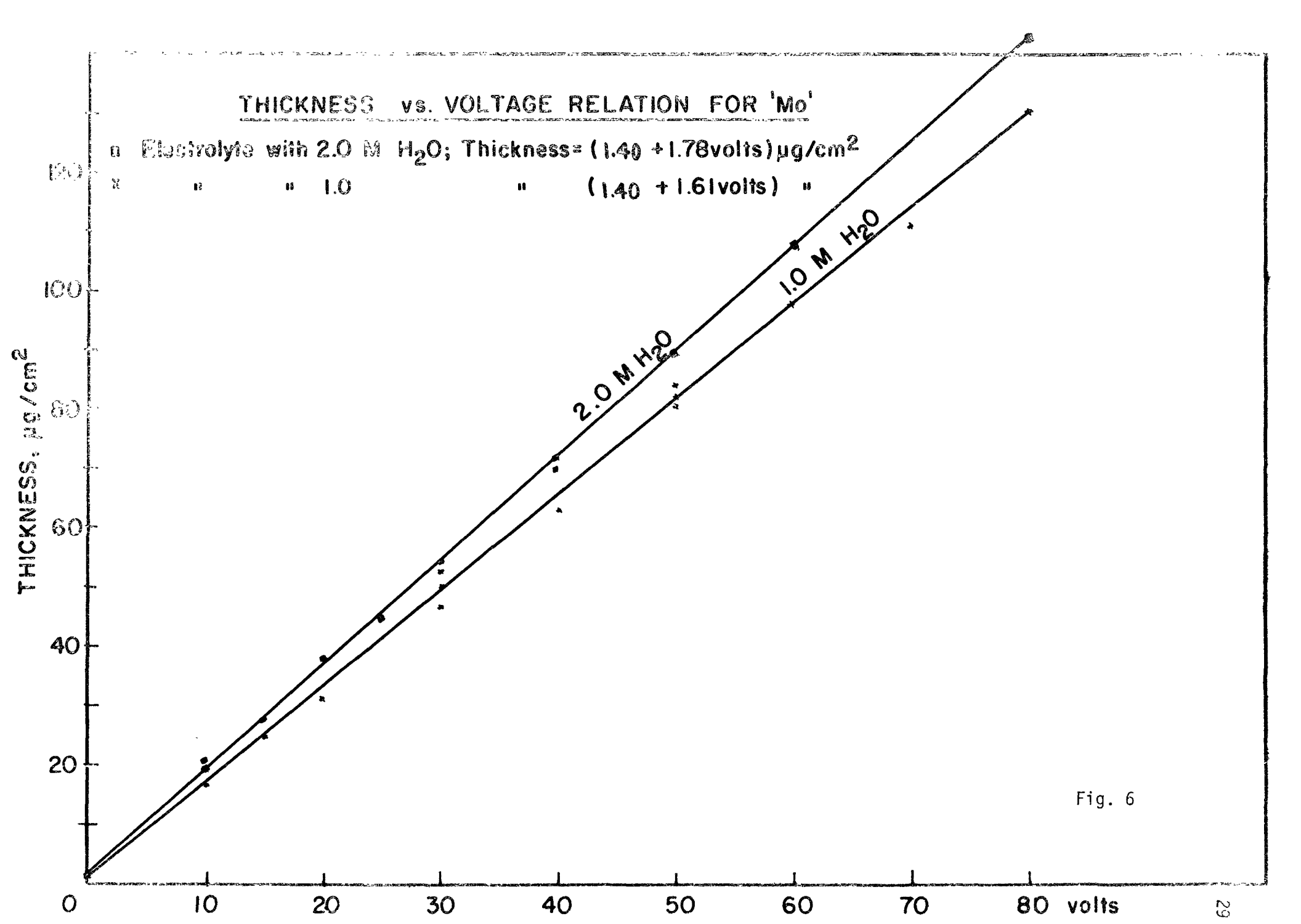
THICKNESS vs. VOLTAGE RELATION FOR 'Mo'
Electrolyte with 2.0 M H_2O; Thickness = (1.40 + 1.78volts) µg/cm²
" " 1.0 " (1.40 + 1.61volts) "
2.0 M H_2O
1.0 M H_2O
THICKNESS, µg/cm²
0
20
40
60
80
100
0
10
20
30
40
50
60
70
80 volts

Fig. 6

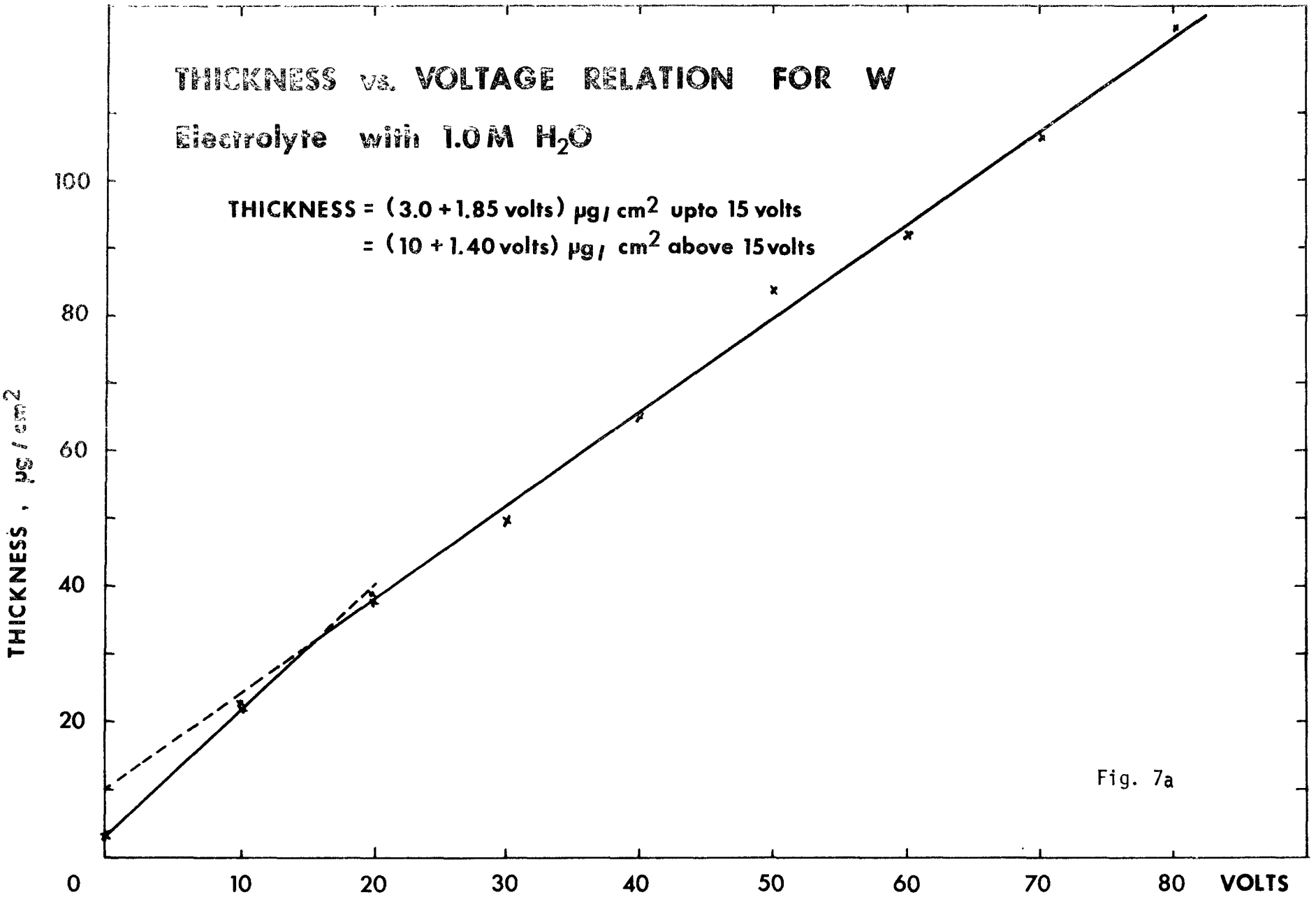
THICKNESS vs. VOLTAGE RELATION FOR W
Electrolyte with 1.0 M H_2O
THICKNESS = (3.0 + 1.85 volts) $\mu g / cm^2$ upto 15 volts
= (10 + 1.40 volts) $\mu g / cm^2$ above 15 volts
THICKNESS , $\mu g / cm^2$
0
20
40
60
80
100
10
30
50
70
VOLTS

Fig. 7a

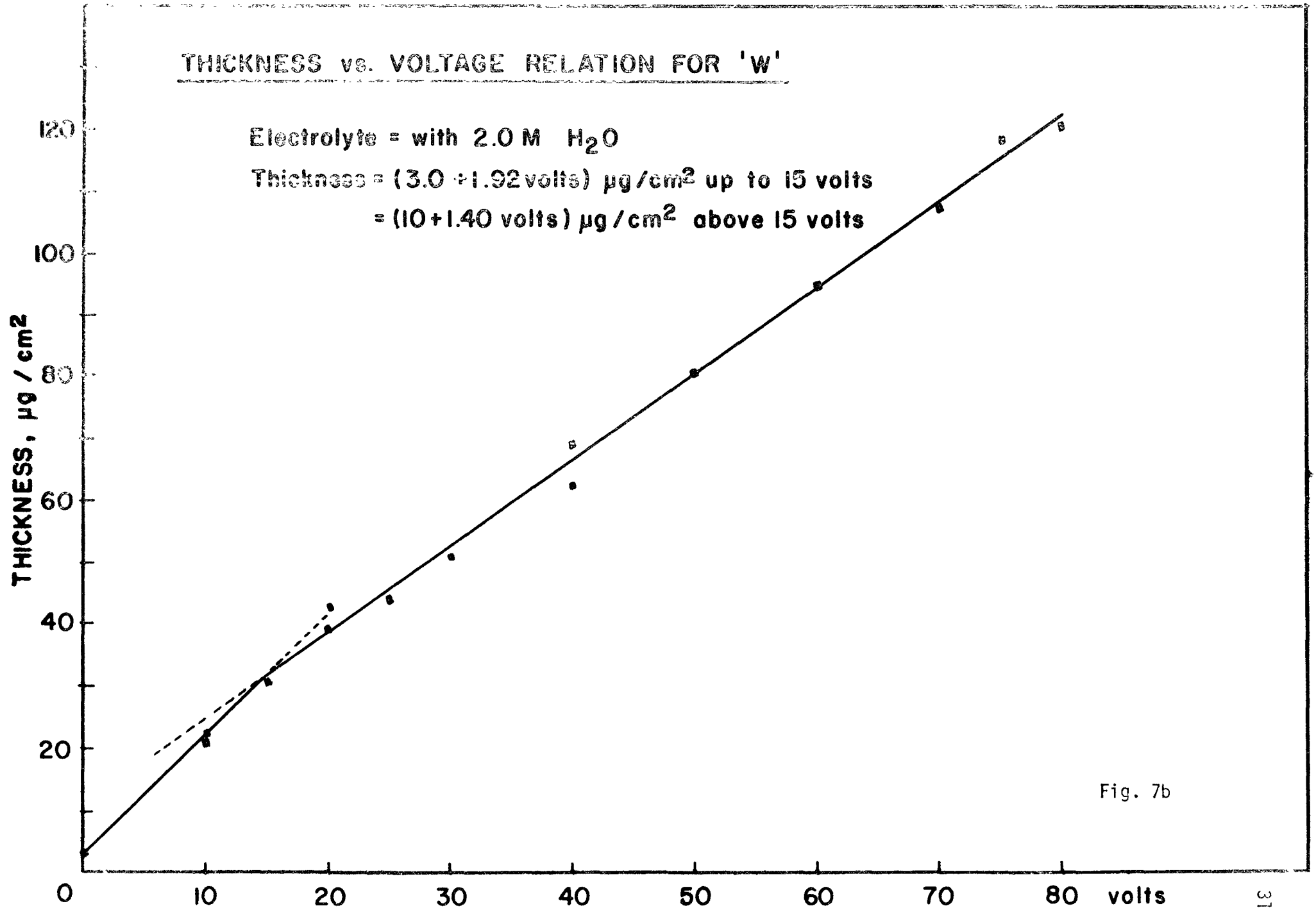
THICKNESS vs. VOLTAGE RELATION FOR 'W'
Electrolyte = with 2.0 M H_2O
Thickness = (3.0 +1.92volts) μg/cm² up to 15 volts
= (10+1.40 volts) μg/cm² above 15 volts
THICKNESS, μg / cm²
120
100
80
60
40
20
0
10
20
30
40
50
60
70
80
volts

Fig. 7b

that contained in the oxide film. However, it is possible that some metal ions may escape into the solution during anodizing. This would cause the total metal removed to be somewhat greater than that indicated in Table I. Therefore, a series of runs was carried out with Mo to investigate the existence and importance of this effect and the results are shown in Fig. 8. It is seen that the dissolution is most significant at low voltages and its relative significance decreases at higher voltages. Analytical expressions for the total metal removed and the metal removed as a part of the oxide film alone, are given as follows:

$$\text{Total Mo removed} = (7.5 + 1.0 \text{ volts}) \ \mu g/cm^2 \quad \text{above 7 volts}$$

$$\text{Mo removed via film} = (0.94 + 1.07 \text{ volts}) \ \mu g/cm^2$$

The water content of the electrolyte is here 1.0M.

2.5.3 Stripping

Anodic films on V and Mo, like those on W (4), were found to dissolve readily in a dilute solution of potassium hydroxide. The stripping was complete within one minute and, of fundamental importance, did not continue into the metal. This was confirmed by implanting radioactive Kr^{85} at 15 keV into the specimens, then anodizing them at 10 volts, and finally exposing the specimens for various time intervals to 0.1 g/liter potassium hydroxide solution. The results thus obtained are given in Table II (cf. 4)

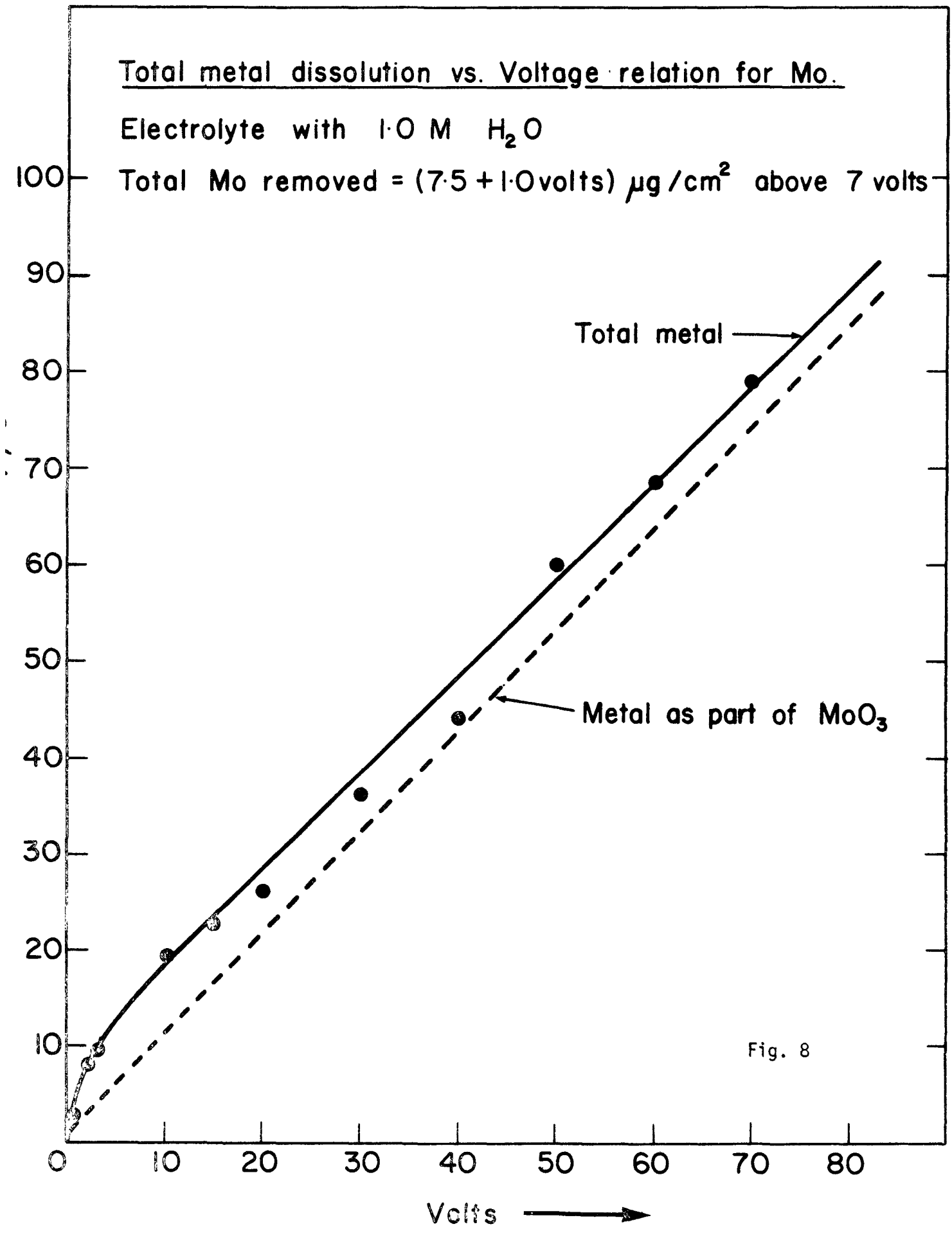
Total metal dissolution vs. Voltage relation for Mo.
Electrolyte with 1·0 M H_2O
Total Mo removed = (7·5 + 1·0 volts) μg/cm² above 7 volts
Total metal
Metal as part of MoO_3
100
90
80
70
60
50
40
30
20
10
0
10
20
30
40
50
60
70
80
Volts

Fig. 8

TABLE II

Time	Normalized-Activity	
	V	Mo
Initial	100	100
15 sec.	57.7	67.6
30 sec.	55.0	59.7
1 min.	50.6	52.5
3 days	49.8	52.6

2.5.4 Constant-Current Film Growth

The growth curves obtained at 25±1°C using various formation current densities and with an anode-cathode separation of 1.0 cm. are shown in Fig. 9 - 11. When film growth commenced, the anode potential increased sharply and this initial transient, which varied with current-density and the anode-cathode separation, was attributed to the ohmic potential drop across the anodizing solution. After the initial transient, the potential of the anode increased slowly with time due to the growth of the film. The data of Fig. 9 - 11 may be interpreted in the present context as showing that the anodizing current should be ≥ 1.5ma/cm^2 in order to minimize the anodizing time.

Ideally, the voltage should rise linearly with time under constant-current conditions. But the experimental current consists of ionic as well as electronic contributions. In the event that the ratio of the electronic current to the total current increases with voltage, the curves will be concave down. In the converse case, they would be con-

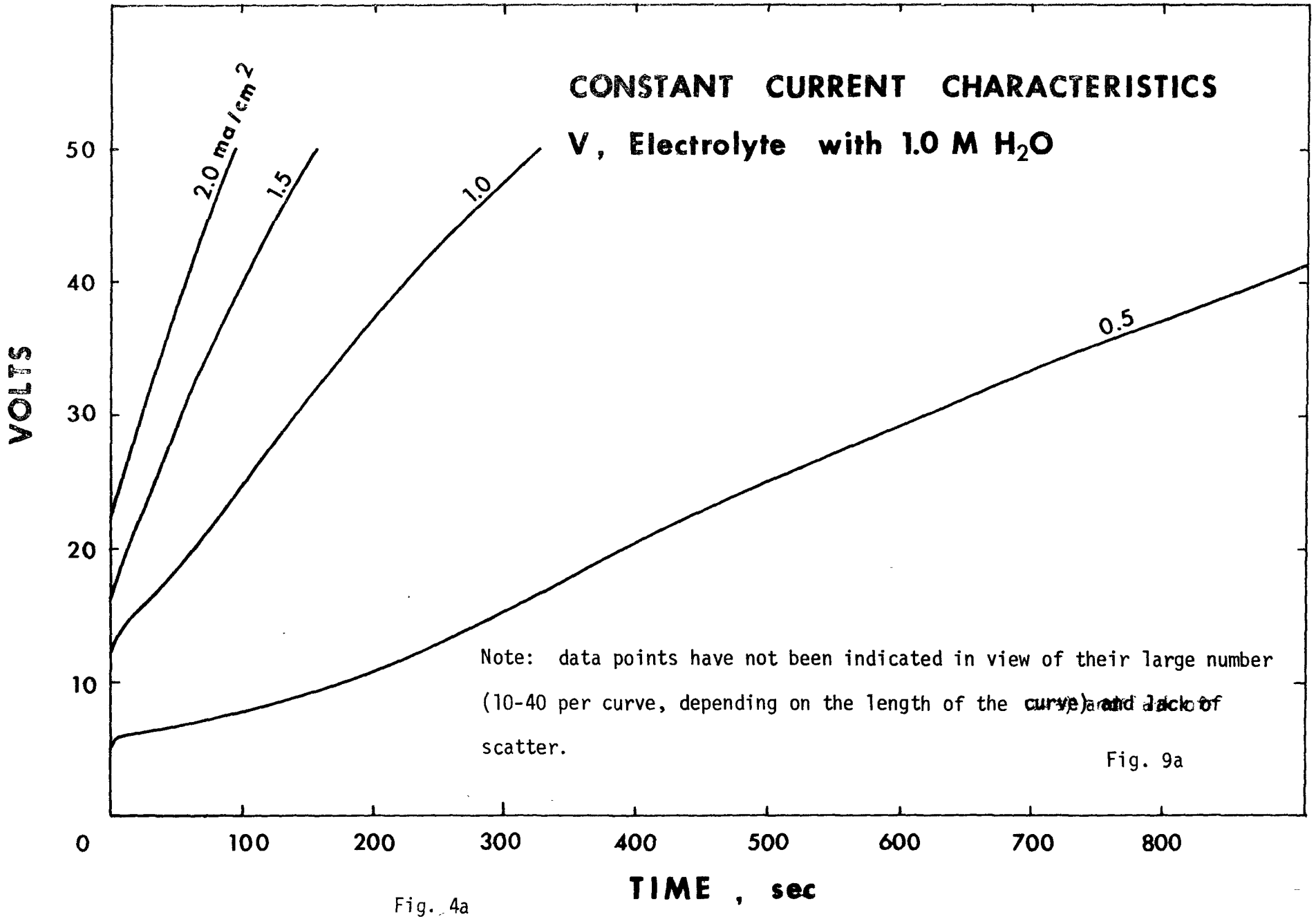

Note: data points have not been indicated in view of their large number (10-40 per curve, depending on the length of the curve) and lack of scatter.

Fig. 9a

Fig. 4a

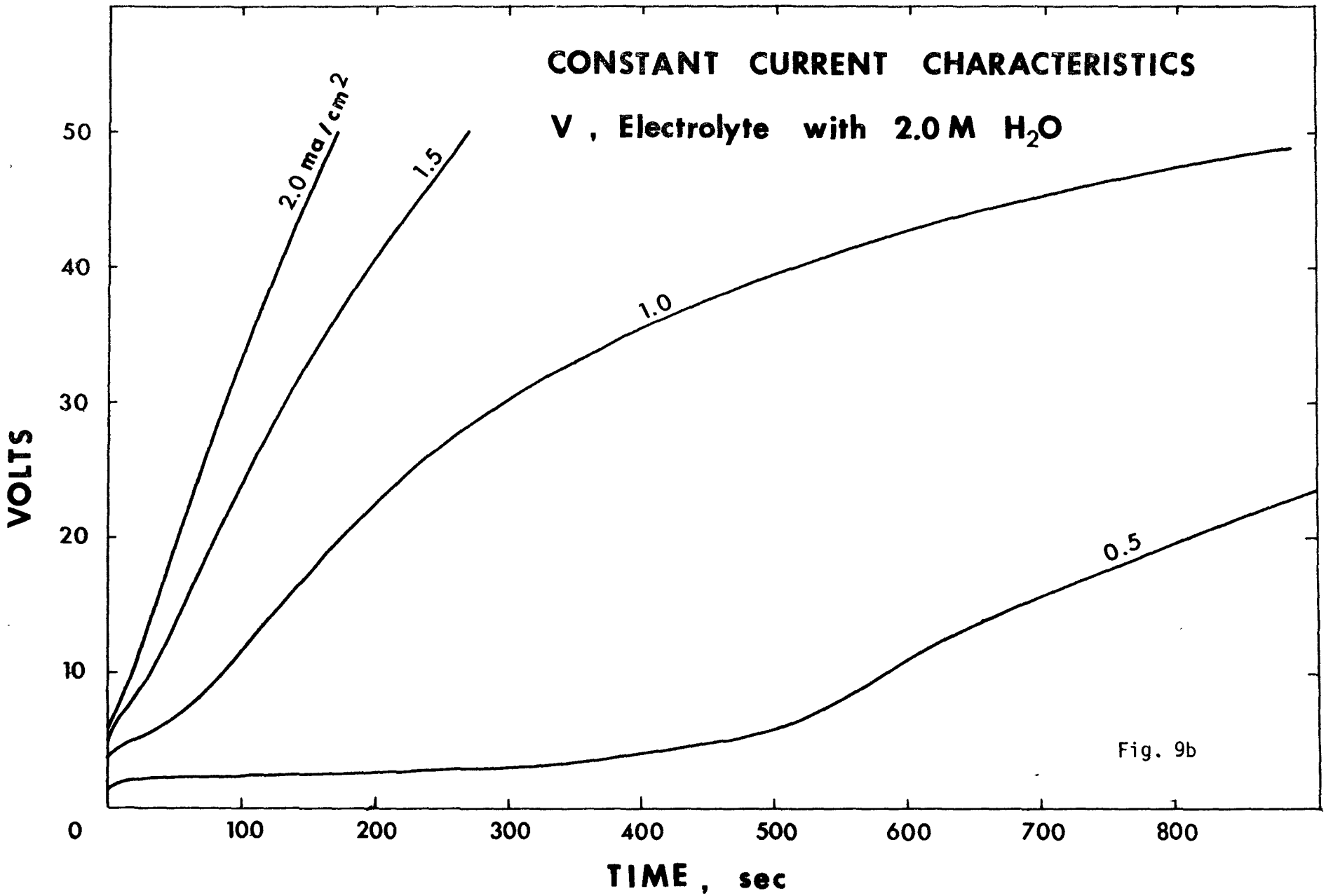
CONSTANT CURRENT CHARACTERISTICS
V , Electrolyte with 2.0 M H_2O
2.0 ma / cm2
1.5
1.0
0.5
VOLTS
0
10
20
30
40
50
100
200
300
400
500
600
700
800
TIME , sec

Fig. 9b

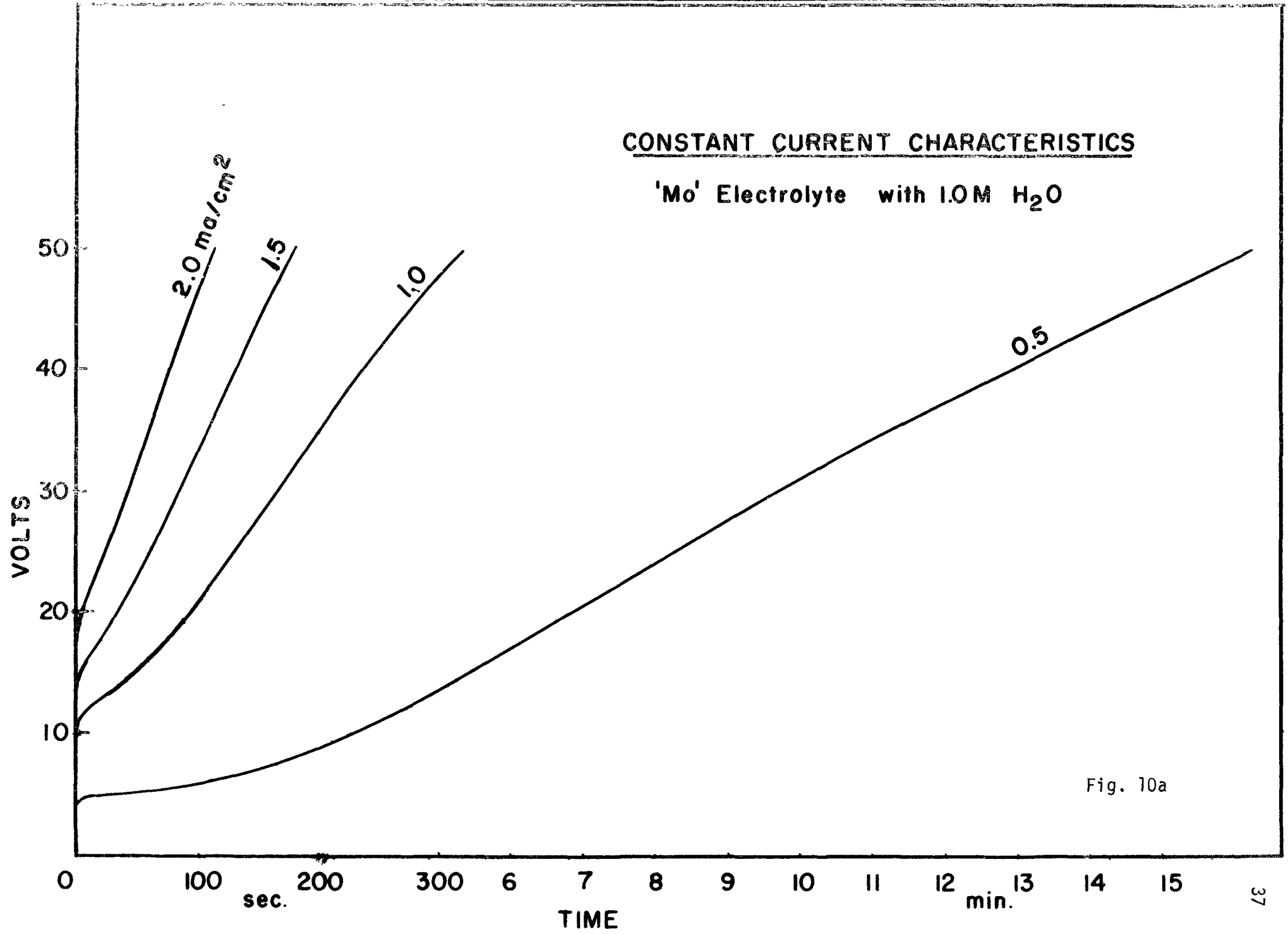
CONSTANT CURRENT CHARACTERISTICS
'Mo' Electrolyte with 1.0 M H_2O
2.0 ma/cm²
1.5
1.0
0.5
VOLTS
50
40
30
20
10
0
100
200
300
sec.
6
7
8
9
10
11
12
13
14
15
min.
TIME

Fig. 10a

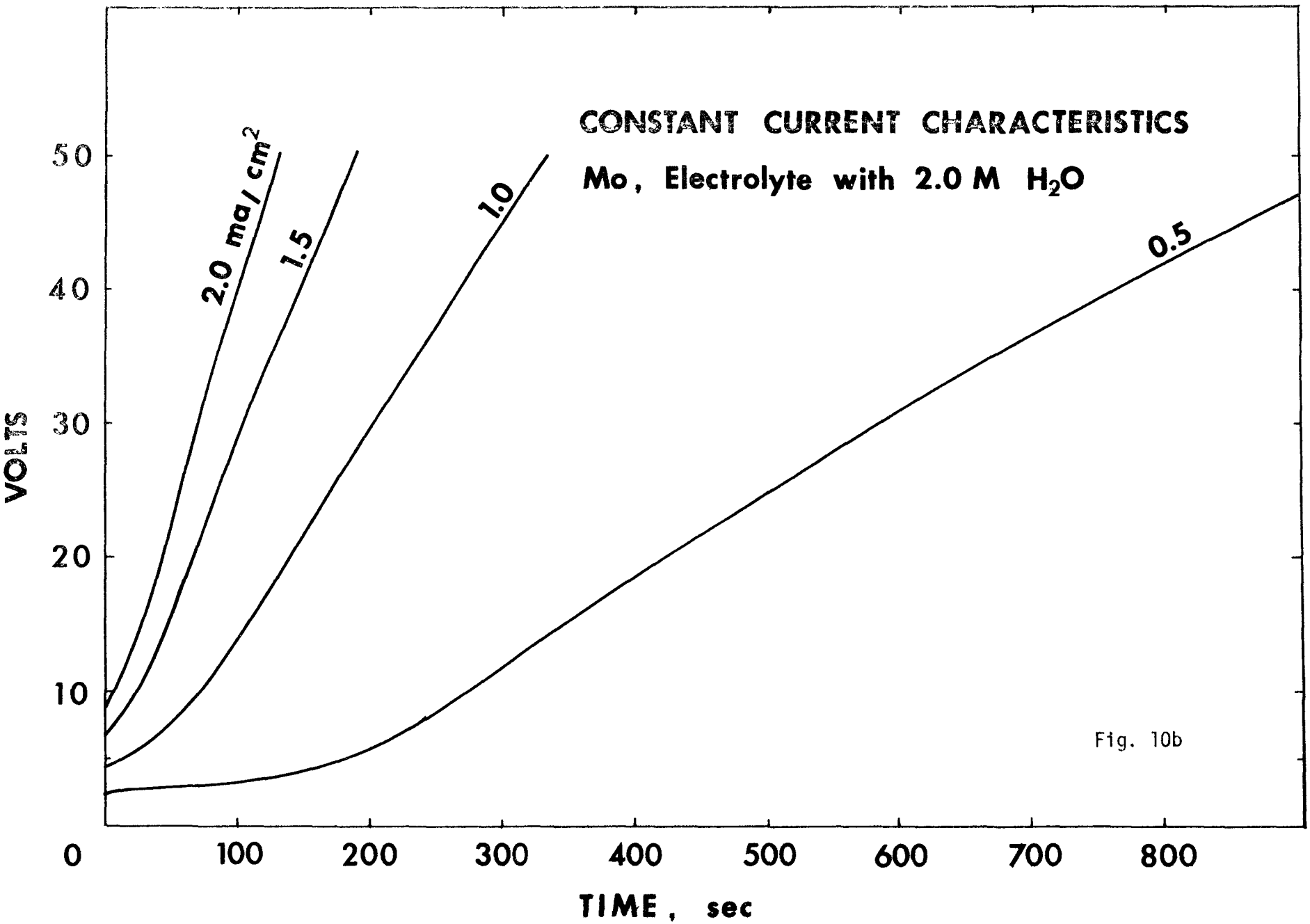
CONSTANT CURRENT CHARACTERISTICS
Mo, Electrolyte with 2.0 M H_2O
2.0 ma/ cm^2
1.5
1.0
0.5
VOLTS
TIME, sec
0
100
200
300
400
500
600
700
800
10
20
30
40
50

Fig. 10b

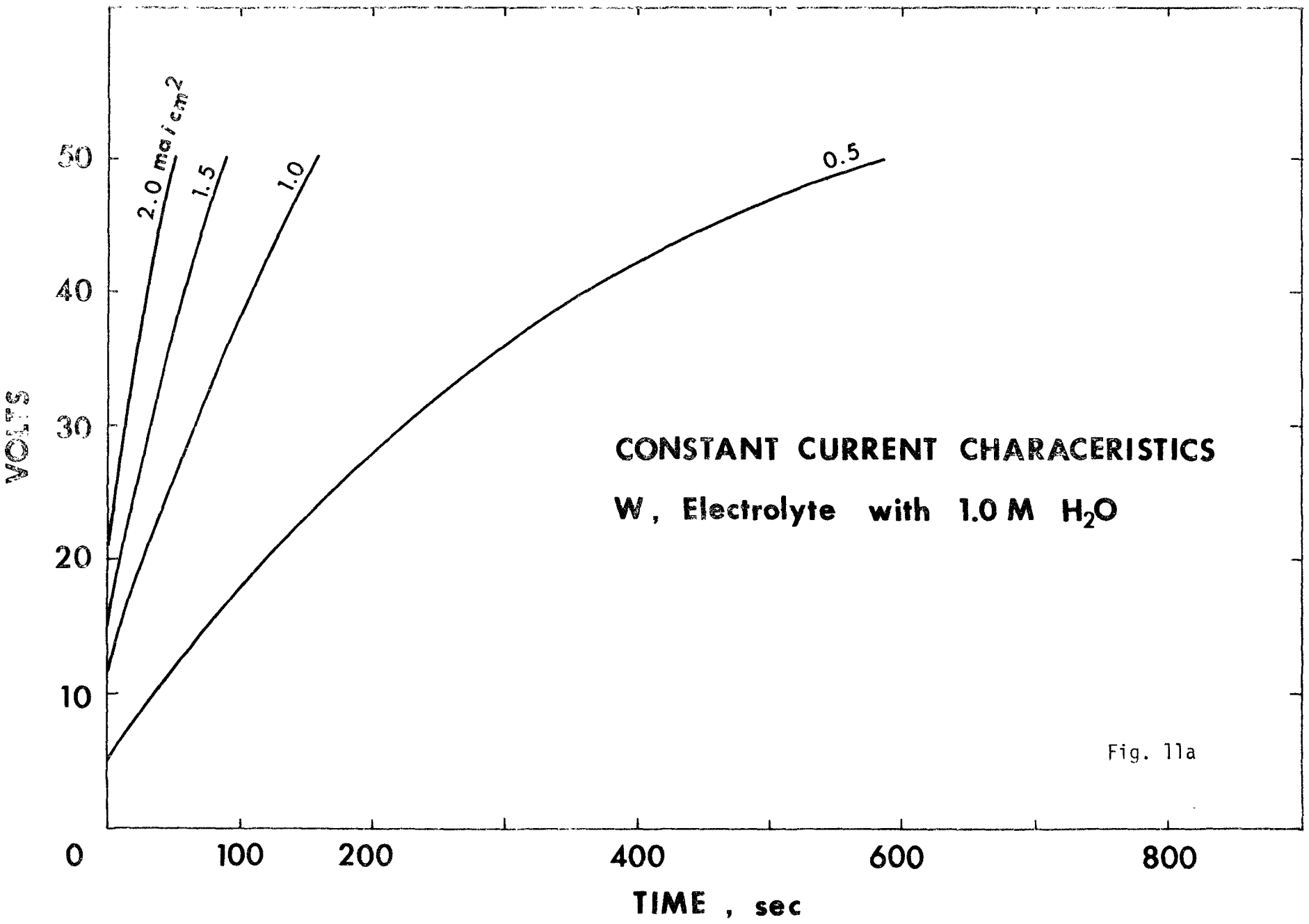
2.0 ma i cm2
1.5
1.0
0.5
50
40
30
20
10
VOLTS
0
100
200
400
600
800
TIME , sec
CONSTANT CURRENT CHARACERISTICS
W , Electrolyte with 1.0 M H2O

Fig. 11a

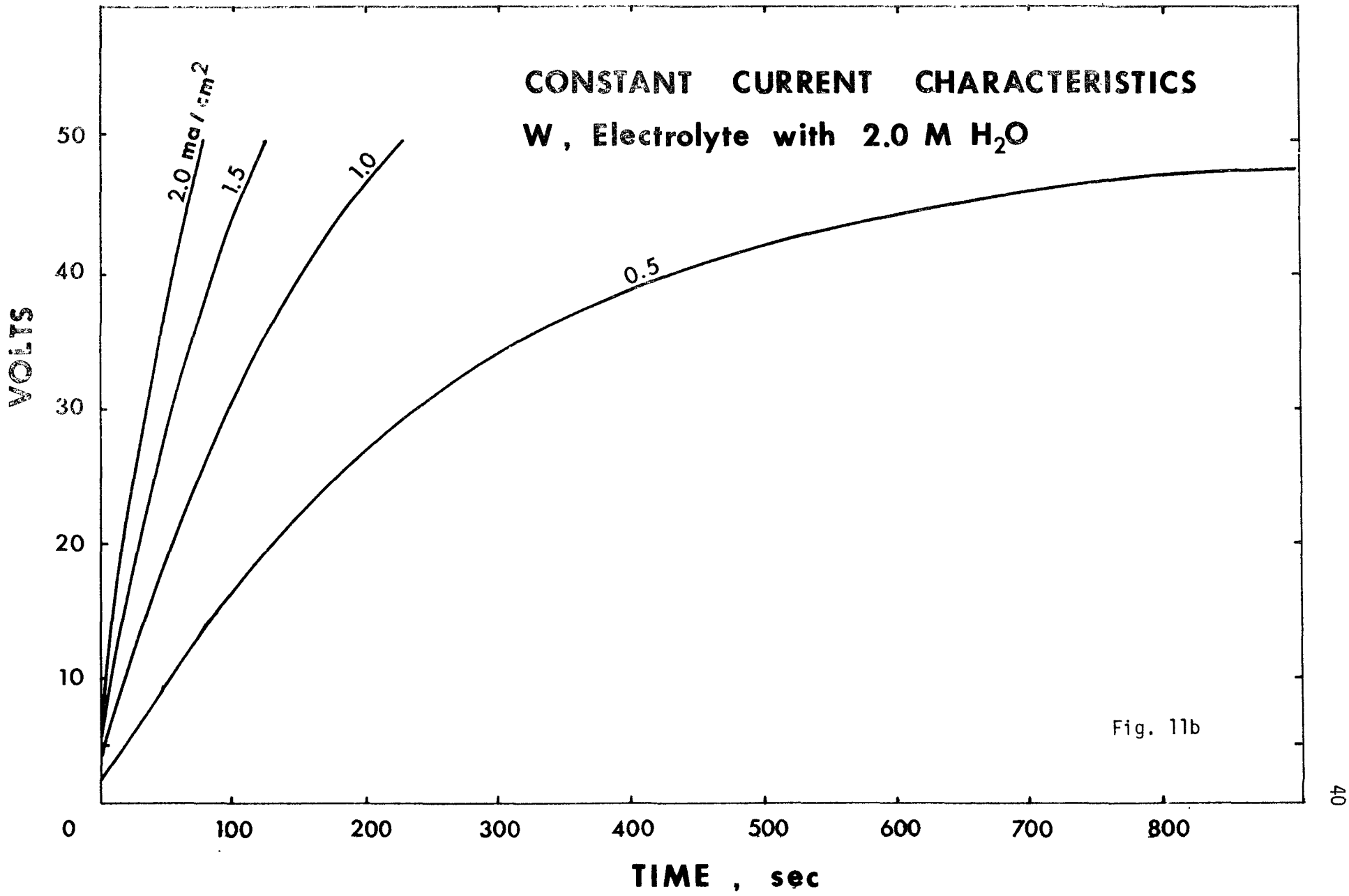
CONSTANT CURRENT CHARACTERISTICS
W , Electrolyte with 2.0 M H_2O
2.0 ma / cm^2
1.5
1.0
0.5
VOLTS
0
10
20
30
40
50
100
200
300
400
500
600
700
800
TIME , sec

Fig. 11b

cave up. In the present work, both situations can be recognized: e.g., in Fig. 9b the 1.0, 1.5 and 2.0 ma/cm^2 curves can be understood in terms of an increasing proportion of the electronic current, while the 0.5 ma/cm^2 curve suggests mainly a decreasing proportion of electronic current.

In an attempt to understand results of this type, we have resorted to further use of ellipsometry. Preliminary measurements show that the density and the stoichiometry of the film may be changing with time; the films seem to become less dense and more non-stoichiometric (i.e., higher k where $\underline{n}$ = n-ik) as they grow thicker. This result can explain the initial slow rise of voltage at 0.5 ma/cm^2 and it certainly accords well with the concave-down behavior found at 1.0, 1.5 and 2.0 ma/cm^2. Further investigations are being carried out.

During the constant-current conditions of film growth, the potential of the anode increased until certain film thickness was attained. At that potential, film-breakdown began. The breakdown voltages are given in Table III. Note that the breakdown voltage for W using the present electrolyte is 190 volts ($\sim$275 $\mu g/cm^2$) while it was found to be about 80 volts ($\sim$87 $\mu g/cm^2$) by McCargo et al (4) using a nitric acid-potassium nitrate electrolyte. The present electrolyte is thus ideally suited for range studies with ions of MeV energies, this being previously not possible.

TABLE III

	Water Content of Electrolyte	Breakdown voltages, volts	Oxide Thickness	
			$\mu g/cm^2$	°A
V	1.0 M	140	154	3540
	2.0 M	110	152	3500
Mo	1.0 M	235	380	8360
	2.0 M	215	384	8500
W	1.0 M	190	275	4040
	2.0 M	190	275	4040

2.5.5 Analysis of the Constant-Current Data

During the film formation at constant ionic current, each new layer of thickness dx requires an extra potential dV to be added across the film to maintain the field in the oxide and hence the current. The quantity dV/dx or E_d may be called the differential field strength. If the potential fall in the already existing part of the film is not changed during further growth, dV/dx is the actual field strength in the new layer just being laid down. We will assume in what follows that dV/dx does not vary with increasing thickness of oxide at constant ionic current density, nor with the ionic current itself. In partial support of this, we would point out that Young (27) has suggested that E_d varies quite slowly with ionic current, usually less than 10% for a tenfold change in the ionic current.

The relation between the rate of rise of potential and the ionic current density is derived as follows. The rate of increase of thick-

ness is given by

$$\frac{dx}{dt} = \frac{iM}{zF\rho} \tag{18}$$

where x = thickness, cm

t = time, sec.

i = ionic current density, amp/cm^2

z = number of Faradays (F) required to form the formula weight of oxide M,

ρ = density of the film, g/cm^3

The rate of increase of potential is therefore

$$\frac{dV}{dt} = E_d \cdot \frac{dx}{dt} = \frac{iME_d}{zF\rho} \tag{19}$$

In equation 19, for a given composition of the oxide, only E_d and ρ are truly unknown, so that knowing one (for example ρ), the other (E_d) may be estimated. These estimates may be checked independently using the weight-loss measurements given in Figs. 5 - 7 and Table I. Thus, knowing the thickness in $\mu g/cm^2$ per volt from these data and using the relation

$$\frac{\mu g}{cm^2} \times \frac{100}{\rho} = {}^{\circ}A \tag{20}$$

we can verify the correctness of E_d or ρ. The problem, however, becomes more complicated when the composition of the oxide is not known with any great certainty. In that case, use may be made of the fact that E_d/ρ is essentially independent of ρ and M/z may then be determined using Eqn. 19. This then leads to the identification of the oxide composition. E_d and ρ can then be determined separately only by having some independent measurements such as ellipsometry.

Only the data using the electrolyte containing 1.0 M water have been analyzed.

We know that the experimental current density has two components, ionic and electronic, defined by

$$I = i + e$$

where I = Total current density

i = ionic current density

e = electronic current density

Assuming that under constant-current conditions of oxide formation, the ratios E_d/ρ and M/z are independent of thickness and the current density, we find from Eqn. 19 that

$$\frac{dV}{dt} \alpha\ i = k(I - e)$$

Using the constant-current characteristic plots given in Figs. 9 - 11, we find the following for 'e' at 25 volts and 50 volts.

TABLE IV

Metal	'e' ma/cm^2	
	25 V	50 V
V	0.32	0.30
Mo	0.16	0.24
W	0.14	0.33

Thus, 'e' is a significant part of I, i.e., of the experimental current density.

The following data are also available:

MoO_x: $\frac{dV}{dx} = E_d = 2.86 \times 10^6$ volts/cm corresponding to 35°A/volt as determined directly by ellipsometry*; composition assumed to be MoO_3, thence z = 6.

WO_x: $\rho = 6.80$ g/cm^3 (27); composition assumed to be WO_3, thence z = 6.

Then, using equation 19 and the estimates of the electronic current 'e' at 25 volts, we get the following, where known quantities are underlined.

TABLE V

Metal	z	ρ_{oxide} g/cm^3	E_d volts/cm x 10^6	$\frac{1}{E_d} = \frac{dx}{dV}$ °A/volt	$\frac{1}{E_d}$ from Figs 5-7
Mo	6	4.52	<u>2.86</u>	<u>35.0</u>	35.0
W	6	<u>6.80</u>	4.81	20.8	20.6

It is seen from the above Table that there is good agreement between the constant-current data and the weight-loss measurements for Mo and W. Such a result would therefore seem to confirm the assumed compositions, densities and differential field strengths for anodic films on Mo and W. Since independent values of E_d or ρ were not available for the oxide film on V, such calculations could not be made. However, it was still possible to take advantage of the fact that E_d/ρ may be assumed to be a constant. The ratio M/z was accordingly estimated for V, and was found to be 18.1 as compared to 18.2 and 20.75 for V_2O_5 and VO_2

* Private communication from Mr. Colin Rowe, McMaster University, Hamilton.

respectively. The implication is that the oxide formed on V by anodizing is V_2O_5.

However, these calculations were based on the estimations of 'e' from the slopes of V-t curves given in Figs. 9 - 11; these slopes involve a possible error of up to 10-15% which leads to an error of 3 - 5% in the values of i and hence in those of M/z. An uncertainty of 5% in the value of M/z = 18.1 means that M/z might have been 19.0, corresponding to z = 4.61. This means that there is some ambiguity in the composition of the anodic oxide films on V; it seems to be somewhere between VO_2 and V_2O_5. More definite values for z, E_d and ρ cannot be ascertained from the available data.

2.5.6 Constant-Voltage Film Growth

Anodic films were also grown under constant voltage conditions, the anode-cathode separation being again 1 cm. Typical characteristic curves, obtained at 50 volts, are shown in Figs. 12-14. The initially large current density across the electrode surface as the film growth commenced decreased rapidly until it reached an almost limiting value of 0.1-0.4 ma/cm^2.

We would first of all point out that the limiting currents agree in general with the values established in section 2.5.5 for the electronic current. Such agreement is important in showing the self-consistency of the interpretation.

The constant-voltage curves also lead to a tentative identification of the anodic film compositions, just as was possible with the constant-current curves in section 2.5.5. Thus, the area under these curves gives the total charge passed in forming the films at 50 volts;

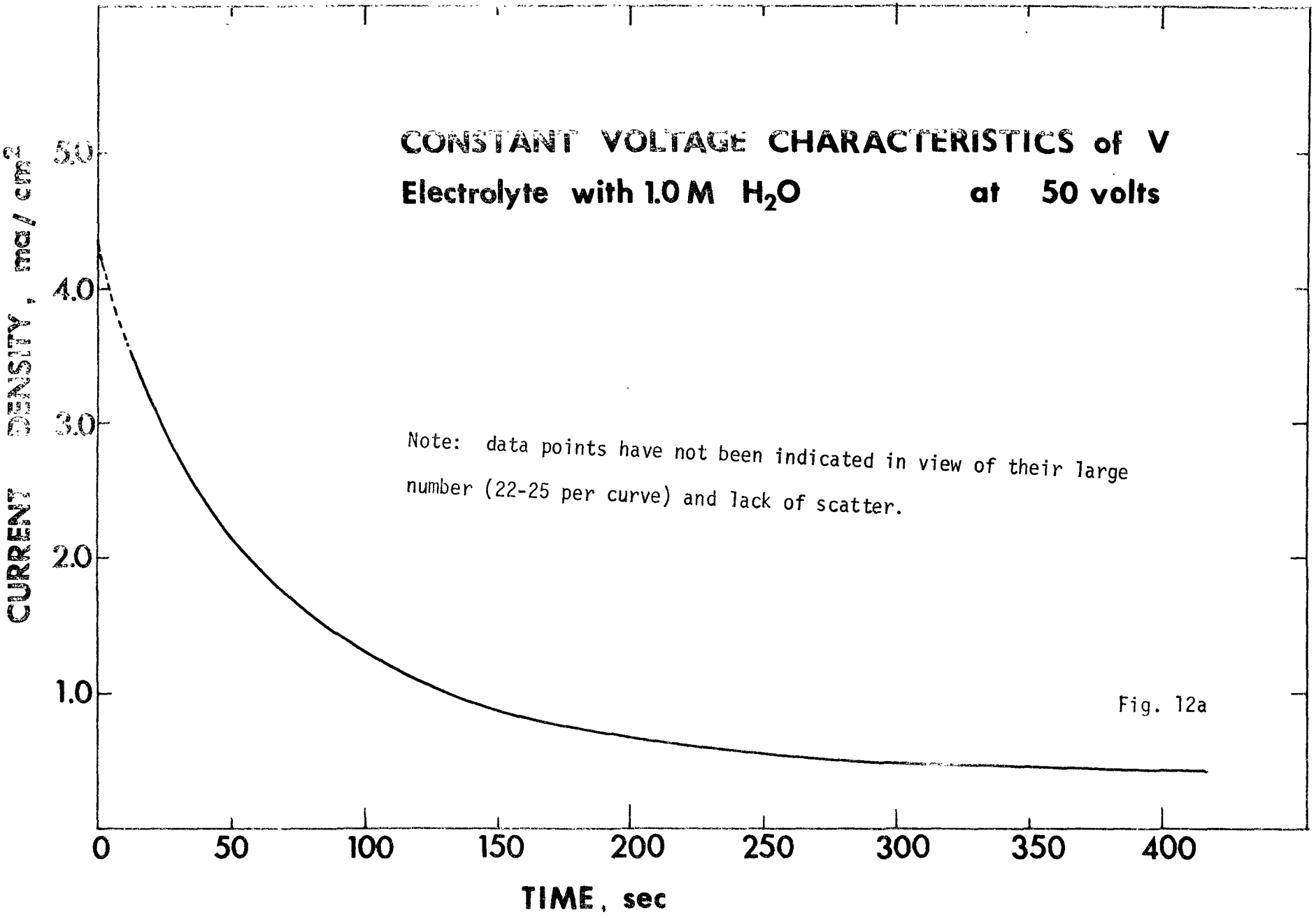
CONSTANT VOLTAGE CHARACTERISTICS of V
Electrolyte with 1.0 M H_2O at 50 volts
Note: data points have not been indicated in view of their large number (22-25 per curve) and lack of scatter.
CURRENT DENSITY, ma/cm²
5.0
4.0
3.0
2.0
1.0
0
50
100
150
200
250
300
350
400
TIME, sec

Fig. 12a

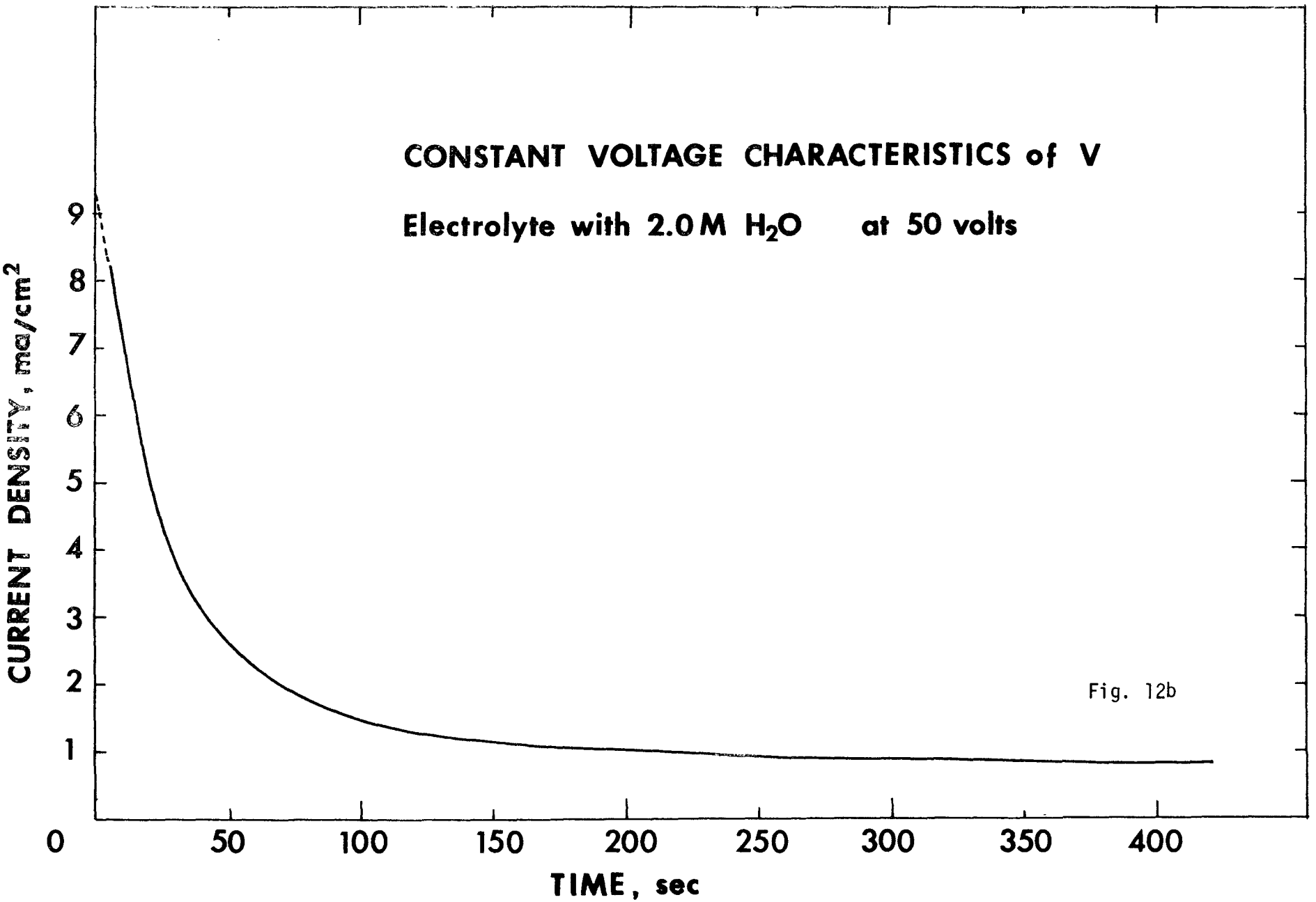
CONSTANT VOLTAGE CHARACTERISTICS of V
Electrolyte with 2.0 M H_2O at 50 volts
CURRENT DENSITY, ma/cm^2
9
8
7
6
5
4
3
2
1
0
50
100
150
200
250
300
350
400
TIME, sec

Fig. 12b

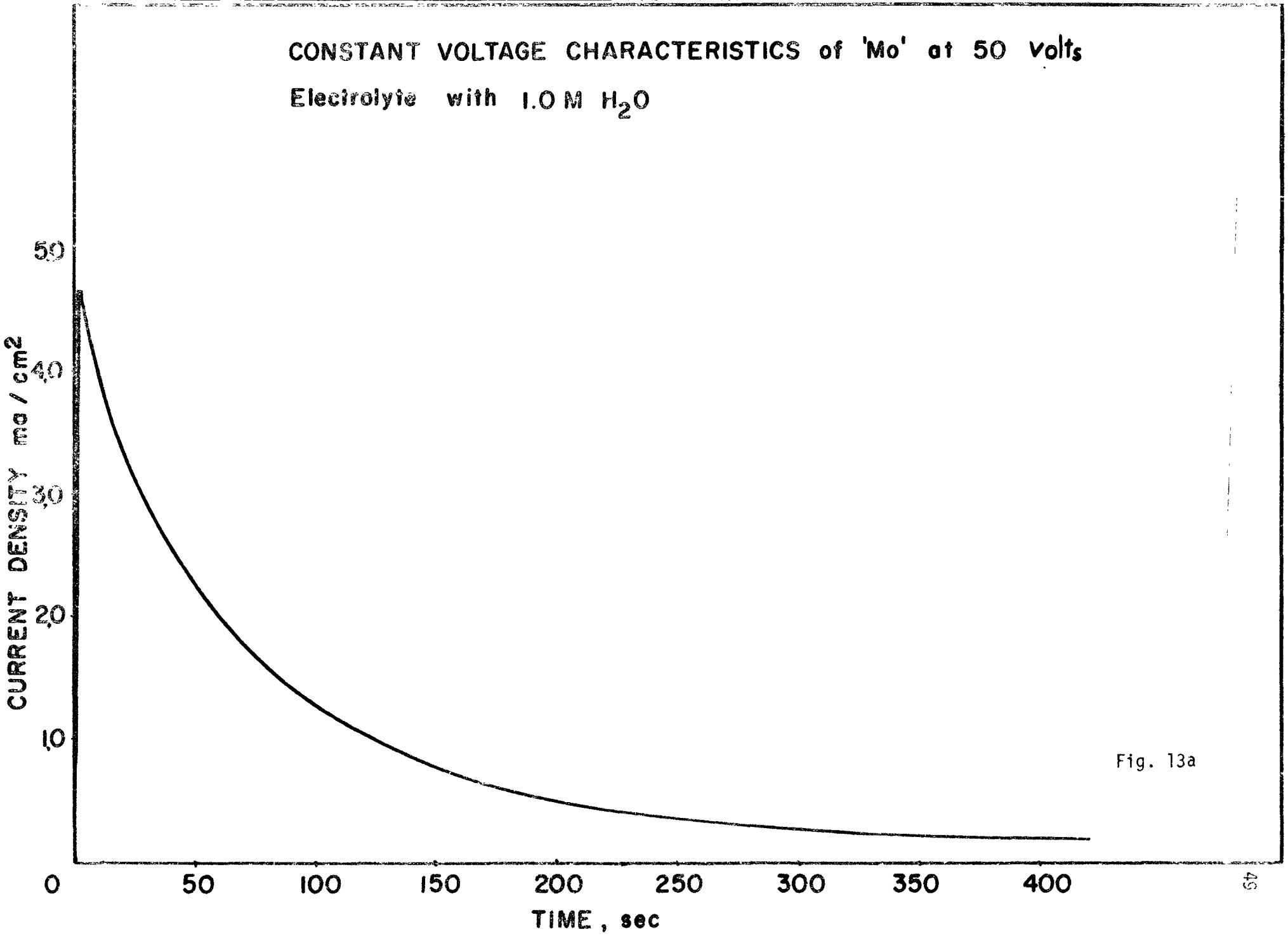
CONSTANT VOLTAGE CHARACTERISTICS of 'Mo' at 50 Volts
Electrolyte with 1.0 M H_2O
CURRENT DENSITY ma / cm²
50
40
30
20
10
0
50
100
150
200
250
300
350
400
TIME , sec

Fig. 13a

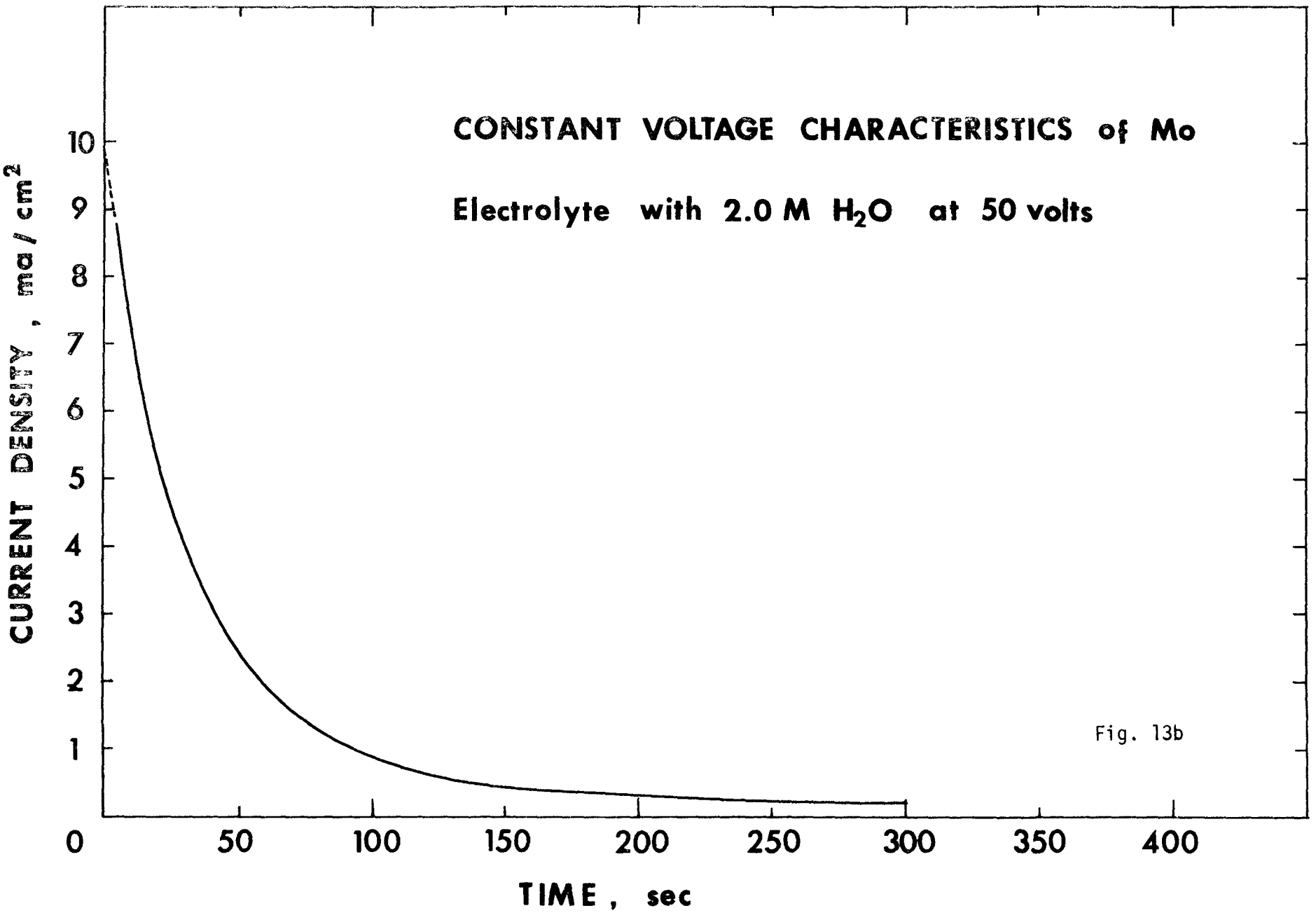

Fig. 13b

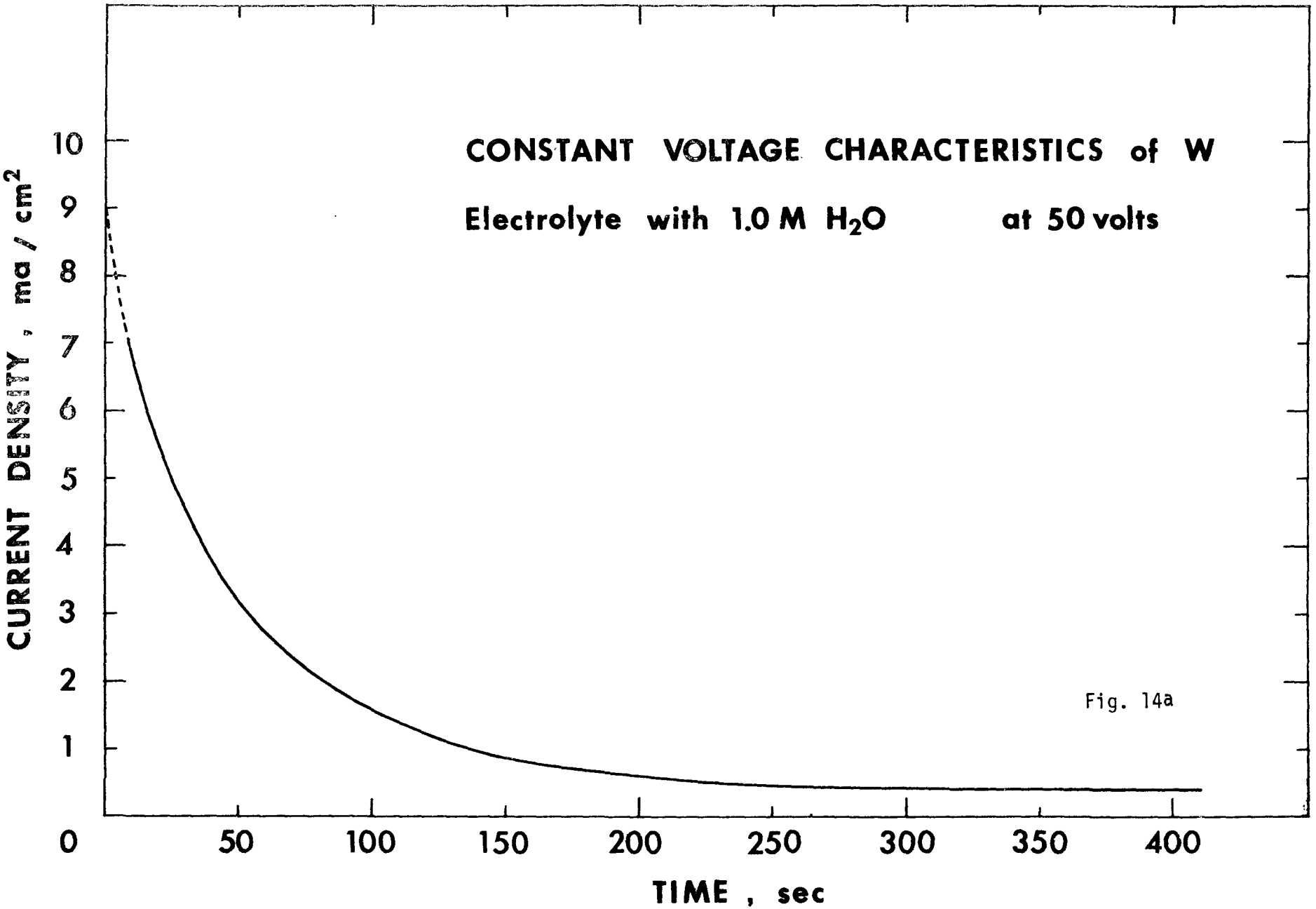
CONSTANT VOLTAGE CHARACTERISTICS of W
Electrolyte with 1.0 M H_2O at 50 volts
CURRENT DENSITY , ma / cm^2
TIME , sec
0
1
2
3
4
5
6
7
8
9
10
50
100
150
200
250
300
350
400

Fig. 14a

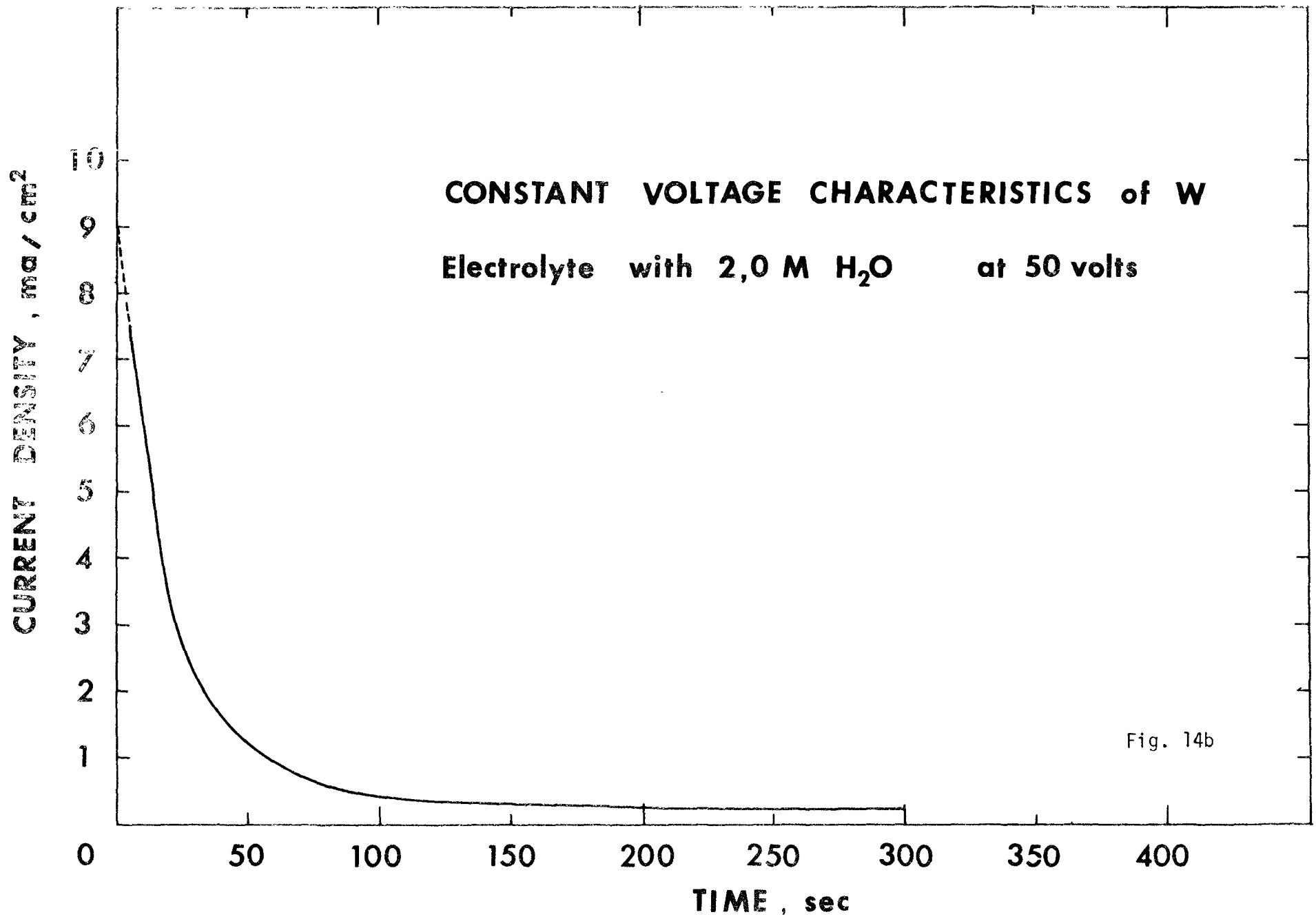
CONSTANT VOLTAGE CHARACTERISTICS of W
Electrolyte with 2,0 M H_2O at 50 volts
CURRENT DENSITY , ma / cm²
TIME , sec
0
50
100
150
200
250
300
350
400
1
2
3
4
5
6
7
8
9
10

Fig. 14b

by assuming various film compositions, coulombic charge calculations give the thickness (in $\mu g/cm^2$) of the films, which can be compared with the film thickness obtained from weight-loss measurements. In making such calculations, it was assumed that the remaining current after six minutes of anodizing is due to electrons and that the continuing contribution from ionic current is nil. This assumption tends to make lower limits of the film thicknesses obtained from the coulombic charge calculations. Results are given in Table VI.

TABLE VI

	Electrolyte: 1M H_2O 0.02 M Sodium Borate in Acetic Acid	
	Voltage: 50 volts	
	Film Thickness, $\mu g/cm^2$	
	Coulombic charge calculations	Weight-loss measurements
V	$VO_2 \geq 55.6$	55.2
	$V_2O_5 \geq 50.6$	
Mo	$MoO_2 \geq 104.0$	81.6
	$MoO_3 \geq 77.5$	
W	$WO_2 \geq 111.5$	80.0
	$WO_3 \geq 80.0$	

We conclude once again that anodic films should be respectively MoO_3 and WO_3 for Mo and W, but that for V there is a basic uncertainty.

2.5.7 Conclusions

In summary, anodic films formed at either constant current or constant voltage are known to be extremely uniform (42) and since, in the cases of Mo and V, a dilute solution of potassium hydroxide dissolves only the anodic films without affecting the targets, it has thus become possible to remove uniform layers of known thicknesses, up to an accuracy of ±10°A, from the surfaces of Mo and V. This technique will now be used in determining the depth-distributions of energetic Kr ions in polycrystalline Mo.

CHAPTER 3

Depth Distributions of Energetic Kr^{85} in Polycrystalline Mo

3.1 Theory

3.1.1 General

As mentioned earlier, due to experimental difficulties, depth-distributions are known only for a relatively limited number of energetic ion-target combinations. In the absence of measurements, the most generally accepted way of obtaining range data is by means of the theoretical treatment of Lindhard, Scharff and Schiøtt (43). This is based on a model in which the energy loss occurs by nuclear and electronic stopping (treated as additive) and where the arrangement of atoms in the target is assumed to be random. Because the role of crystal structure is ignored, their results apply strictly only to amorphous targets and not to crystalline materials, whether polycrystalline or single-crystalline.

3.1.2 Stopping Processes

When energetic ions, 5-200 KeV, are injected into a solid, there are two main competing energy-loss processes: elastic collisions between the incident ions and the target nuclei, also called nuclear collisions; inelastic collisions between the incident ions and the target electrons, also called eletronic excitation.

Nuclear Collisions Incident ions may be scattered in the screened

coulomb fields of target nuclei and the momentum imparted to the struck atoms is often sufficient to permanently displace them from their equilibrium positions. As seen in Fig. 15*, the stopping cross-section for nuclear collisions is large for low ion velocities and therefore nuclear stopping can be expected to be the dominant stopping process near the end of the incoming ion's range regardless of its initial velocity.

Electronic Excitation The injected ion may also lose energy by ionizing or exciting target electrons. This process is important at the higher energies (cf. Fig. 15) where incident ion and target electrons have similar velocities and is therefore most significant for light and fast-moving ions during their initial slowing down.

3.1.3 Range Concepts

The Total Range:

The total range, R, is defined simply as the sum of the path lengths between successive collisions. Owing to the statistical nature of the collision processes, however, there is a spread in total ranges and an average total range, $\overline{R}$, may be defined as the arithmetic average as would be observed with a large number of incident particles.

The Projected Range:

$R_{proj.}$ is the average penetration depth as projected along the normal to the target surface. It is $R_{proj.}$ rather than $\overline{R}$ which is observed experimentally.

The Most Probable Range:

$R_{prob.}$ is the most probable projected penetration depth, i.e., the peak, if any, in the differential range profile.

* ρ and ε in Fig. 15 are defined on p. 61.

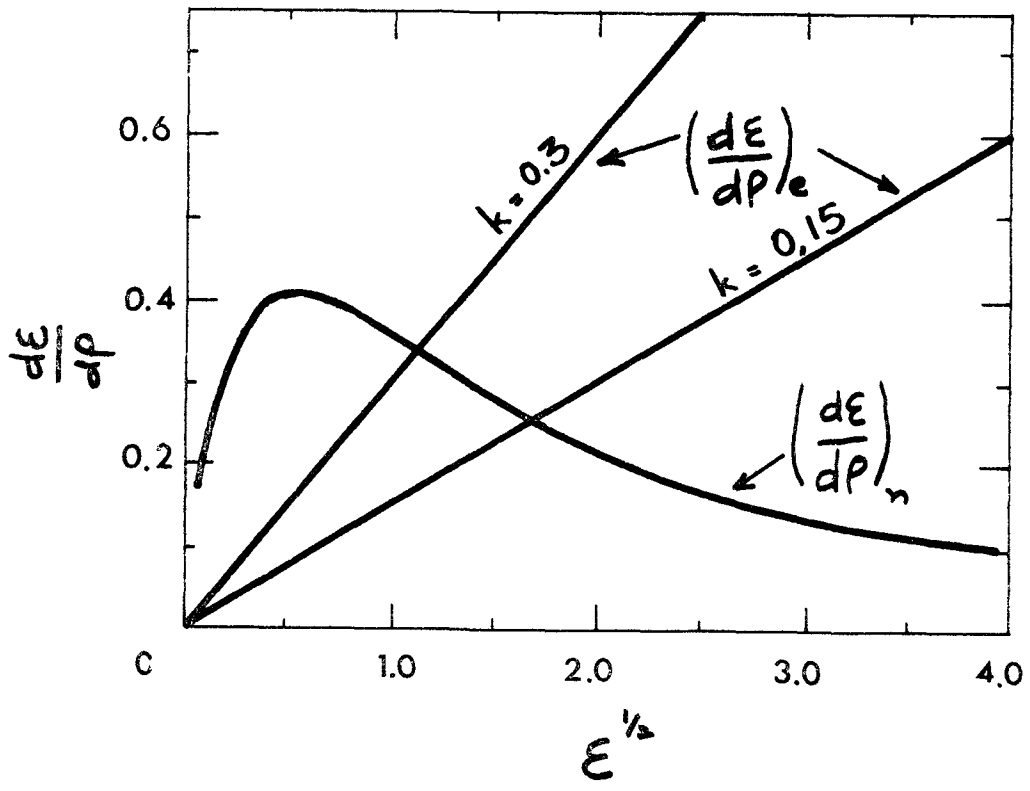

NUCLEAR & ELECTRONIC STOPPING POWERS IN ρ-ε UNITS

Fig. 15

The Median Range:

$R_{med.}$ is the median projected penetration depth, i.e., the range within which 50% of the ions are brought to rest.

The Maximum Range:

$R_{max.}$ is the upper limit for ion penetration as observed for the small fraction of ions which suffer no nuclear collisions due to motion in crystallographically open directions (channelling).

In amorphous substances, the range profile resembles a gaussian distribution, so that $R_{proj.}$, $R_{prob.}$ and $R_{med.}$ are nearly equivalent (to within roughly 20%). The occurrence of channelling in crystalline solids causes the profile to broaden asymmetrically towards deeper penetration (i.e. towards $R_{max.}$), and significant deviations between the three types of ranges can then arise. Where channelling is minimal, however, an appreciable departure from the amorphous case is expected only for $R_{proj.}$. Consequently, range estimates derived from the work of Lindhard (43) et al for use with crystalline targets are most meaningfully identified with $R_{prob.}$ or $R_{med.}$.

3.1.4 The Theory of Lindhard, Scharff and Schiøtt (43)

This theory assumes the collisions to be two-bodied, classical, and non-relativistic, and employs a Thomas-Fermi interaction potential for predicting energy-loss during collisions. The energy loss per unit path length for a moving ion can, in accordance with what we have said before, be split up into two contributions which are, to first approximation, additive:

$$\frac{dE}{dx} = \left(\frac{dE}{dx}\right)_e + \left(\frac{dE}{dx}\right)_n \tag{21}$$

$$\equiv -N[S_e(E) + S_n(E)]$$

$$\equiv -NS(E) \tag{22}$$

where $S_e(E)$ = stopping cross-section for energy loss to electrons

$S_n(e)$ = stopping cross-section for energy transformed to nuclear motion

N = number density of atoms in the target

The quantity $S(E)$ is in turn related to $d\sigma$, the differential scattering cross-section, by the integral:

$$S = \int_0^{\Lambda E} T d\sigma$$

where T = transferred energy

$$\Lambda = \frac{4M_1M_2}{(M_1+M_2)^2}$$

M_1, M_2 = mass of incident ion and of target respectively

This description by stopping and scattering cross-sections is adequate for random media, i.e., when crystal lattice effects (channelling) can be ignored. It leads immediately to a direct estimate of the mean total range,

$$\overline{R} = -\int_0^E \frac{dE}{\left(\frac{dE}{dx}\right)_e + \left(\frac{dE}{dx}\right)_n} \tag{23}$$

which takes on a particularly simple form in the limits of low and high energy.

At Low Energy

Since, according to Ref. 7

$$\left(\frac{dE}{dx}\right)_e = KE^{1/2} \tag{24}$$

electronic stopping is quite small as compared to nuclear stopping at low enough energy (cf. also Fig. 15), and so,

$$\overline{R} \simeq \int_0^E \frac{dE}{NS_n} \tag{25}$$

For a power law type of differential scattering cross-section, we have (44)

$$d\sigma = CE^{-m}T^{-1-m}dT$$

and therefore,

$$S_n = \int_0^{\Lambda E} T d\sigma$$

$$= \frac{C}{1-m} \Lambda^{1-m} E^{1-2m} \tag{26}$$

where

$$C = \frac{\pi}{2} \lambda_m a^2 \left(\frac{E}{\varepsilon}\right)^{2m} \Lambda^m$$

$$0 < m \leq 1$$

$$\lambda_{1/2} = 0.327, \quad \lambda_{1/3} = 1.19$$

a = Thomas-Fermi screening parameter (45)

ε = defined below

Substituting equation 26 in 25 yields

$$\overline{R} \simeq \frac{(1-m)E^{2m}}{2mC\Lambda^{1-m}N} \tag{27}$$

while multiplying both sides by $\left(\frac{\rho}{R}\right)$, where ρ is defined below, gives

$$\rho = \frac{(1-m)\varepsilon^{2m}}{2mC\Lambda^{1-m}N} \left(\frac{\rho}{R}\right) \left(\frac{E}{\varepsilon}\right)^{2m}$$

and so, $$\rho = \frac{(1-m)}{m\lambda_m}\,\varepsilon^{2m} \tag{28}$$

Here ρ and ε are the dimensionless range parameters of Lindhard, namely,

$$\varepsilon = E\frac{aM_2}{Z_1Z_2e^2(M_1+M_2)} \tag{29}$$

$$\rho = R\frac{NM_2 4\pi a^2 M_1}{(M_1+M_2)^2} \tag{30}$$

where Z_1, Z_2 = atomic number of incident ion and of target, respectively. For a tabulation of ε and ρ, see Winterbon (45). The significance of the ρ-ε notation is seen clearly in Eqn. 28, in that all parameters restricted to a particular ion or target have cancelled out, leaving a result which is essentially universal.

According to Winterbon et al (44), m = 1/2 (corresponding approximately to an inverse-square potential) is a satisfactory approximation for $0.08 \leq \varepsilon \leq 2$, thence over almost the whole keV range, while $m<1/3$ is appropriate for lower energies and m=2/3 for very high energies (ε was not here specified (44)).

Equation 28 becomes, for m=1/2, the well known universal range-energy equation of Nielsen (1)

$$\rho = 3.06\varepsilon \tag{31}$$

At Very High Energy

Since electronic stopping tends to dominate over nuclear stopping at very high energy, we can write

$$\overline{R} \simeq \int_0^E \frac{dE}{NS_e}$$

$$= \int_0^E \frac{dE}{KE^{1/2}}$$

$$= \frac{2E^{1/2}}{K} \qquad (32)$$

In ρ-ε units, equation 32 becomes

$$\rho = \frac{2\varepsilon^{1/2}}{k} \qquad (32A)$$

where

$$k \simeq \frac{0.0793\ Z_1^{2/3}\ Z_2^{1/2}\ (M_1+M_2)^{3/2}}{(Z_1^{2/3}+Z_2^{2/3})^{3/4}\ M_1^{3/2}\ M_2^{1/2}}$$

We note that equation 32A is not quite universal since it depends upon k and so on Z_1 and Z_2; the values taken on by k for most useful ion-target combinations tend,nevertheless, to lie in the narrow interval of 0.1 to 0.2.

General Case

At intermediate energies, where both types of stopping are important, one must write

$$\rho = -\int_0^{\varepsilon} \frac{d\varepsilon}{(d\varepsilon/d\rho)_n + (d\varepsilon/d\rho)_e} = \rho(\varepsilon,k) \qquad (33)$$

and ρ is accordingly neither universal nor has a simple form. Equation 33 has been tabulated extensively by Winterbon (45) for a Thomas-Fermi differential scattering cross-section though has, apparently, never been treated for power-law scattering.

We have stated in section 3.1.3 that the experimentally measured quantity is $R_{proj.}$ rather than $\overline{R}$. Lindhard (43) has given an approximate relation between $\overline{R}$ and $R_{proj.}$ for pure nuclear stopping governed by a power-law differential cross-section with m=1/2, namely

$$\frac{\bar{R}}{R_{proj.}} \simeq 1 + \frac{M_2}{3M_1} \qquad (34)$$

This relation gives good agreement between theory and experiment up to $M_2/M_1 = 2$ and should therefore be valid for the present ion-target combinations of Kr-Mo and Kr-V.

3.1.5 Depth Distribution Profiles Using Edgeworth's Expansion

We define f(x) such that f(x)dx is the probability for a projectile to come to rest in a layer of thickness dx at a depth x from the starting point. In calculating f(x), we assume that f(x) can be approximated with successively increasing accuracy by the use of Edgeworth's expansion in terms of spatial moments over the true range distribution; this expansion converges best when the distribution under consideration is similar to a gaussian, which is the case for amorphous targets with $M_2 > M_1$.

We use the dimensionless parameter ξ, where

$$\xi \equiv \frac{x-\langle x\rangle}{\mu_2^{1/2}}$$

with $$\mu_n = \langle (x-\langle x\rangle)^n \rangle \qquad n=2,3,4,----$$

$f(\xi)$ is then approximated by N terms in Edgeworth's expansion

$$f(\xi) = \sum_{n=2}^{N} a_n(\xi) \qquad (35)$$

where

$$a_2(\xi) = \frac{1}{\sqrt{2\pi}} \exp(-\xi^2/2)$$

$$a_3(\xi) = -\frac{\mu_3}{6\sqrt{2\pi}\cdot\mu_2^{3/2}}(3\xi-\xi^3)\exp(-\xi^2/2)$$

Thus, altogether one can write for the first two terms,

$$f(\xi) \simeq \frac{1}{\sqrt{2\pi}}\exp(-\frac{\xi^2}{2})\left[1 - \frac{\mu_3}{6\mu_2^{3/2}}(3\xi-\xi^3)\right] , \tag{36}$$

where μ_3 would be zero if the distribution were truly Gaussian (44). Equation 36 can be integrated from $\xi(x)$ to ∞ to give

$$\int_{\xi(x)}^{\infty} f(\xi)d\xi = \frac{1}{\sqrt{2\pi}}\int_{\xi(x)}^{\infty} e^{-\xi^2/2}\,d\xi - \frac{1}{2\sqrt{2\pi}}\frac{\mu_3}{\mu_2^{3/2}}\int_{\xi(x)}^{\infty}\xi e^{-\xi^2/2}\,d\xi$$

$$+\frac{1}{6\sqrt{2\pi}}\frac{\mu_3}{\mu_2^{3/2}}\int_{\xi(x)}^{\infty}\xi^3 e^{-\xi^2/2}\,d\xi$$

$$= \frac{1}{2}\,\mathrm{erfc}\left[\frac{\xi(x)}{\sqrt{2}}\right] + \frac{1}{6\sqrt{2\pi}}\frac{\mu_3}{\mu_2^{3/2}}\,e^{-\xi^2/2}[\xi^2-1] \tag{37}$$

Equations 36 and 37 give the theoretical differential and integral concentration profiles, respectively, for energetic ions incident onto amorphous targets. We note that equation 37, being based on an assumed infinite medium, is not quite normalized for a semi-infinite medium. Figure 16 shows the typical form taken by equations 36 and 37.

3.2 Experimental

3.2.1 General

In brief, the experimental method of determining the depth distributions of radioactive ions in solids consists of:

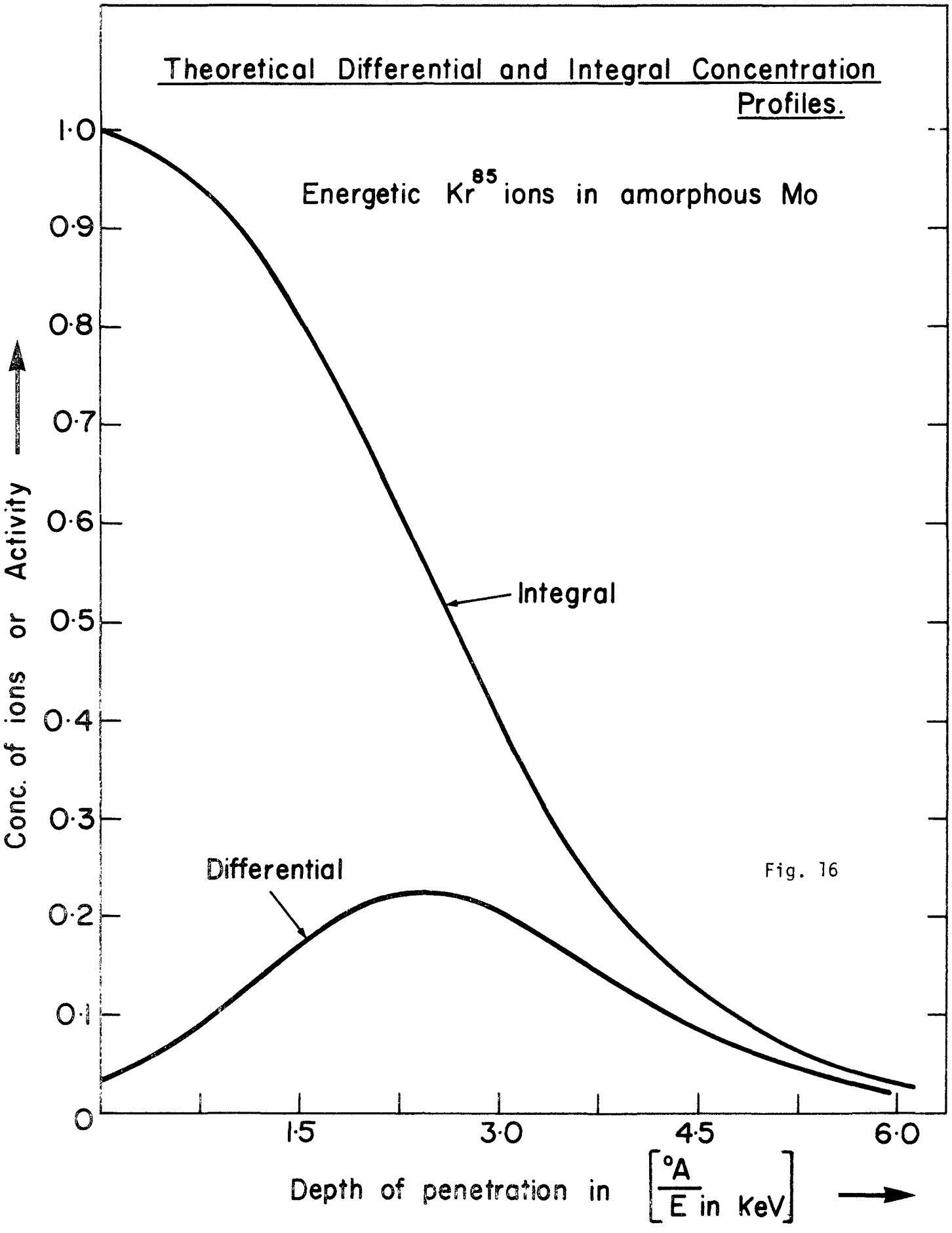
Theoretical Differential and Integral Concentration Profiles.
Energetic Kr^{85} ions in amorphous Mo
Integral
Differential
Conc. of ions or Activity
1·0
0·9
0·8
0·7
0·6
0·5
0·4
0·3
0·2
0·1
0
1·5
3·0
4·5
6·0
Depth of penetration in $\left[\frac{°A}{E \text{ in KeV}}\right]$

Fig. 16

(a) Bombardment of the targets with radioactive ions of chosen energy;

(b) Removal of successive layers from the surface of the target by the two-step process of anodic oxidation (in electrolyte containing 1.0 M water) and film stripping (as described in Chapter 2); and

(c) Counting the target activity both initially and after each anodizing-stripping sequence.

We recall, at this point, that the result of the anodizing-stripping sequence is to remove a thickness of Mo, given by

$$\text{Thickness of Mo removed} = (7.5+1.0 \text{ volts}) \ \mu g/cm^2 \qquad (38)$$

3.2.2 Bombardment and Counting Techniques

All the bombardments in this work were carried out using an ion accelerator constructed in our laboratory by Dr. R. Kelly. It was designed to produce heavy gas ions, such as O_2^+, Ne^+, Kr^+, Xe^+, etc., at energies up to 45 KeV, and at currents varying from 1-100μA. This ion accelerator has no mass separation though it permits suppression of secondary electrons. (The lack of mass separation is to some extent compensated by the exclusive use of heavy ions, since impurities would be of low mass, and would create less damage than what one predicts from their abundance). Fig. 17 shows the target arrangement and Fig. 18 the design of the ion source of radio-frequency type. In this ion source, the anode (aluminum) is designed to dissipate up to 100 watts of electron energy, and a cathode (nickel) with a 1.5 mm canal allows for the extraction of positive ions. The discharge vessel is of pyrex glass and the catnode insulator is sapphire. The purpose of the canal insulator is to shape the plasma boundary, thus causing the emitted ions to be effectively

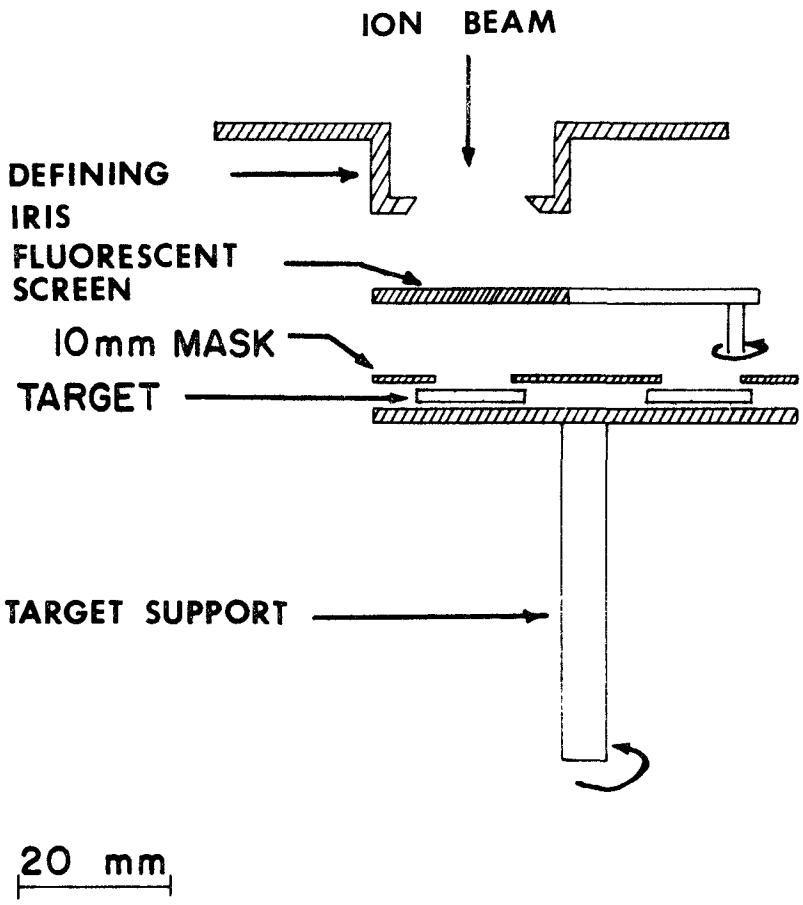

Target Arrangement

Fig. 17

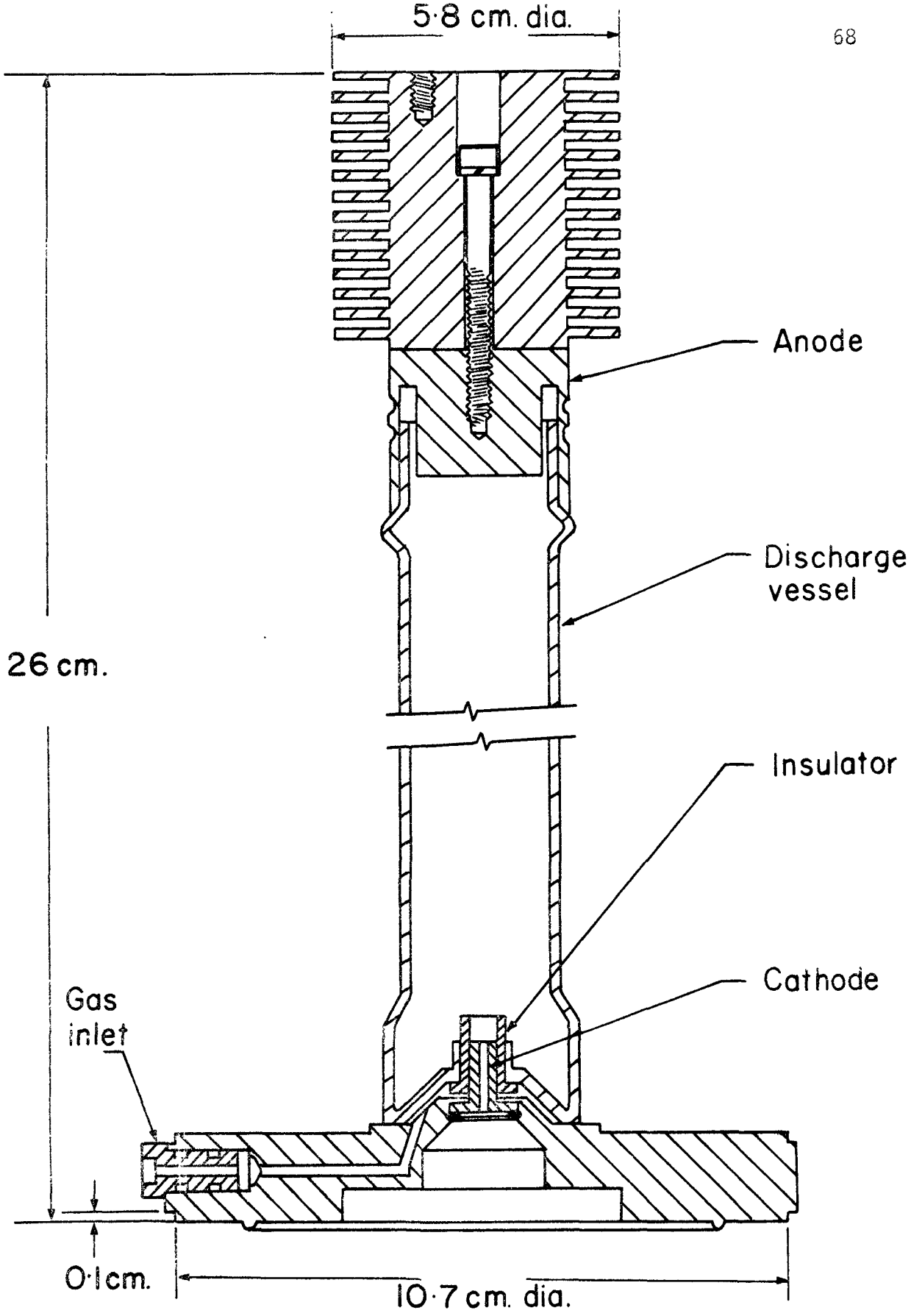

Fig. 18 The Ion Source

focussed into the cathode entrance (47).

The radio-frequency excitation voltage, which is applied externally to the source, originates with an 80 watt, 80 mega-cycle rf oscillator. The rf field within the coil of the oscillator causes electrons to move from wall to wall with the result that the gas in the ion source is partially ionized (48). In addition, a magnetic coil provides an axial magnetic field of 600 gauss near the extraction canal of the cathode. The magnetic field is used firstly to intensify the discharge, by increasing the electron path length so that the electrons are used more efficiently; secondly, it pulls the plasma towards the extraction canal.

Below the discharge vessel, there is a series of focussing electrodes with 14 mm holes which are used to shape the ion beam. A variable positive focussing potential is applied to the focussing electrodes in accordance with whether a small or large beam is required. Though the exact arrangement of the focussing electrodes is somewhat arbitrary, one normally strives to have the sequence of potentials zero-positive-zero as proposed by Pierce (49).

A Faraday cup floating at -850 volts w.r.t. the target is used in order to prevent secondary electrons, which would give current readings too high by a factor of 2 to 3, from leaving the target (an electron leaving the target is electrically indistinguishable from a positive ion striking it). The target is connected to the terminal of a high tension power supply; the particular model used, produced by SAMES (Grenoble), has an internal capacitance of <100 pF and a maximum current of 760 μA; it thus presents virtually no health hazard.

An important component of the ion accelerator system is the vacuum pump used to evacuate the accelerator column. For this purpose, a 4" oil diffusion pump preceded by a liquid nitrogen trap has been chosen, the alternative of ion pumping being unsatisfactory for inert gases. In order to operate properly, the pressure in the accelerator column should be $\leq 10^{-5}$ torr, corresponding to a mean free path of $\geq$ 750 cm. If the pressure is higher, the beam will not be properly focussed and will also be contaminated because of scattering from the residual gas molecules.

The radioactive isotope, Kr^{85}, was obtained from Oak Ridge National Laboratory (Oak Ridge).

The amount of radioactive material in each target was measured using a Philips scalar and GM probe. The particular GM probe had a halogen gas as quenching agent and a mica end-window with a thickness of 3.5 - 4.0 mg/cm^2; it was thus ideally suited for the 675 keV betas emitted by Kr^{85}.

3.3 Results and Discussion

3.3.1 General

The results for a typical range experiment are presented in Table VII. Initial results were found to be anomalous when thick anodic oxide layers were removed from the target surfaces; to circumvent that, oxide layers of smaller thicknesses, formed at up to 3 volts were removed from the targets. Later experiments showed that there was a significant amount of target dissolution during anodizing which resulted in loss of activity to the electrolyte. When this metal dissolution during anodizing

TABLE VII

Distribution of 10 keV Kr^{85} ions in Polycrystalline Mo

Dose = 12.5 μA min/cm^2

Layer No.	Amount of Mo removed: Per layer μg/cm^2*	Amount of Mo removed: Total μg/cm^2	Residual Activity in Target %	Kr^{85} activity per layer calculated from column 4: %	Kr^{85} activity per layer calculated from column 4: % per $\frac{\mu g}{cm^2}$ Mo
1	2	3	4	5	6
	-	-	100	-	-
1	6.75	6.75	71.2	28.8	4.27
2	6.75	13.50	55.3	15.9	2.36
3	6.75	20.25	42.6	12.7	1.88
4	19.1	39.35	20.4	22.2	1.16
5	19.1	58.45	10.45	9.95	0.52
6	19.1	77.55	5.77	4.68	0.245
7	19.1	96.65	2.41	3.36	0.176
8	19.1	115.75	1.62	0.79	0.041
9	19.1	134.85	1.06	0.56	0.029
10	19.1	152.95	0.65	0.41	0.022
11	19.1	173.05	0.51	0.14	0.007
12	19.1	192.15	0.39	0.12	0.006
13	19.1	211.25	0.29	0.10	0.005
14	19.1	230.35	0.24	0.05	0.0026
15	38.2	268.55	0.19	0.05	0.001
16	38.2	306.75	0.105	0.085	0.002

* The three values for layer thickness, 6.75, 19.1 and 38.2 μg/cm^2, correspond respectively to 2 volts (5 min.), 3 volts (12 min.), and 3 volts (24 min.). They thus involve a calibration different from Fig. 8 or equation 38.

was correctly taken into account (see Section 2.5.3), the results were found to be quite consistent, and, in particular, it was not necessary to restrict oneself to low-voltage layers as in Table VII.

Typical distribution curves of residual target activity (column 4, Table VII) for Kr^{85} ions injected into polycrystalline Mo at various bombardment energies and doses are illustrated in Figs. 19 and 20 respectively.

3.3.2 Comparison with Theory

Comparisons of the ranges obtained from these experiments with the theoretical ranges based on Lindhard's theory (section 3.1) have been made both on Figs. 19 and 20 and also in Table VIII. We note a large discrepancy, somewhat similar in extent to that reported for Al and W targets. Significantly, previous observations of the discrepancy include results for Rn injected into W (21), where the mass ratios are similar to Kr in Mo.

TABLE VIII

Energy (KeV)	$R_{proj.}$ ($\mu g/cm^2$)	
	Experimental	Theoretical (Eq. 33 and 34)
5	6	2.4
10	14	3.8
20	20	6.1
30	28	8.3

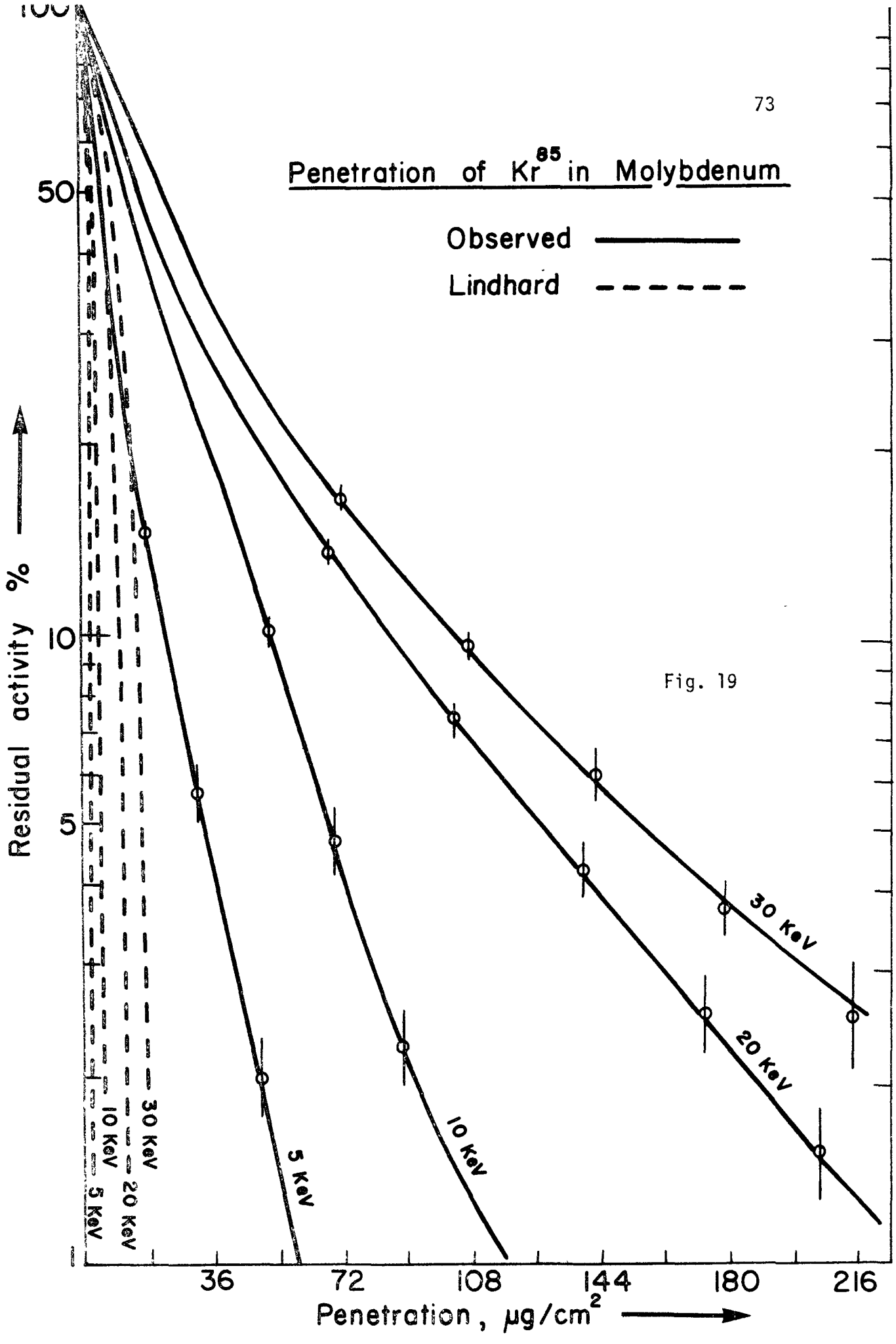
Penetration of Kr85 in Molybdenum
Observed
Lindhard
Residual activity %
50
10
5
30 KeV
20 KeV
10 KeV
5 KeV
36
72
108
144
180
216
Penetration, µg/cm2

Fig. 19

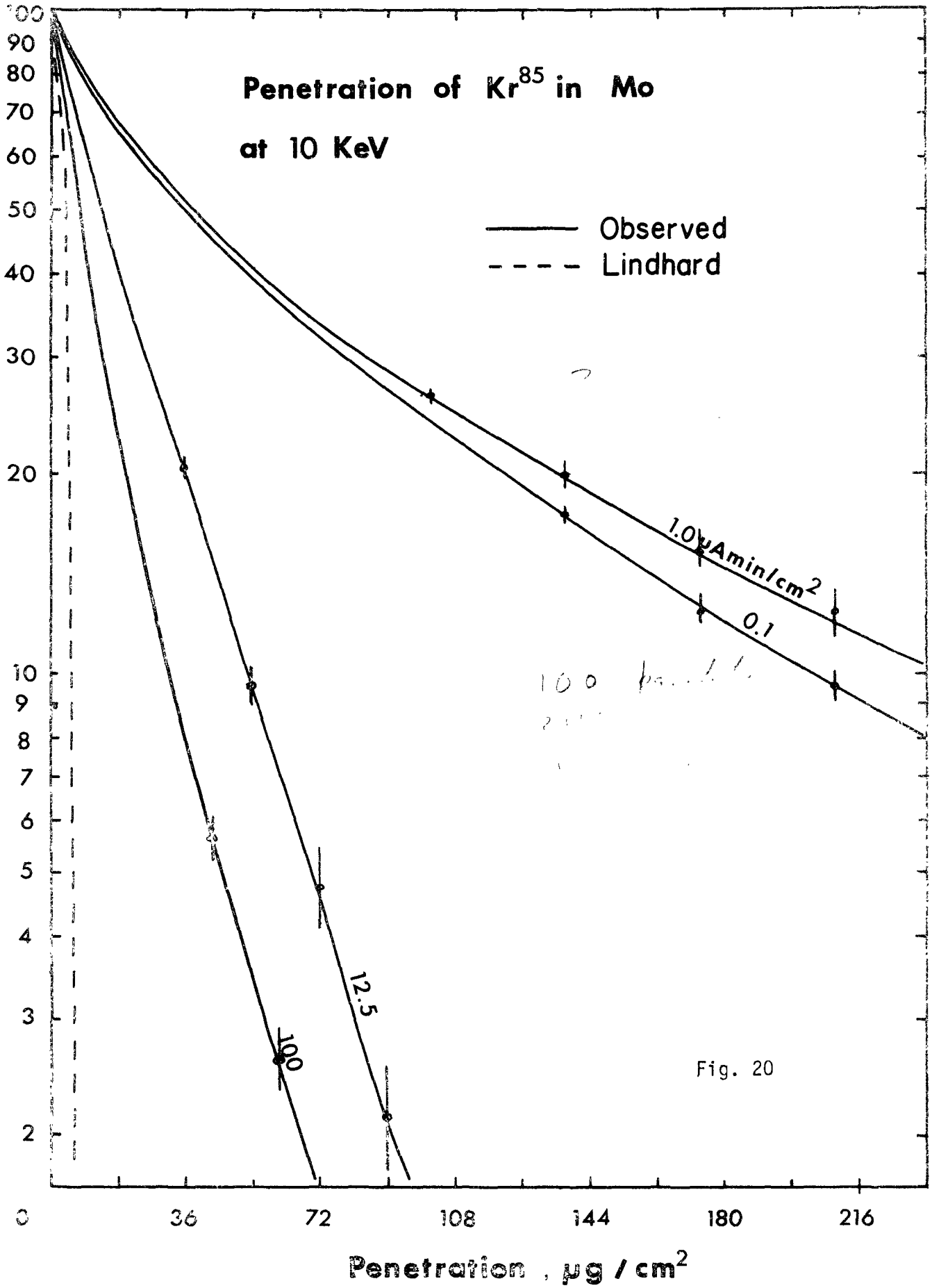
Penetration of Kr85 in Mo
at 10 KeV
Observed
Lindhard
1.0 μAmin/cm2
0.1
12.5
100
100
90
80
70
60
50
40
30
20
10
9
8
7
6
5
4
3
2
0
36
72
108
144
180
216
Penetration , μg / cm2

Fig. 20

The theoretical ranges are based, as we have seen in Section 3.1, on the assumption that the target is amorphous; the large difference between the experimental and the theoretical ranges is therefore tentatively attributed to the crystal lattice effects (cf. 50). Thus, a fraction of the energetic ions when incident upon a crystalline target can get into the open spaces between the rows of atoms and penetrate deep into the solid without encountering as many random collisions as the other ions. These open spaces between the rows of atoms are called "channels" and the phenomenon of deep penetration is called "channelling".

3.3.3 Evidence for Channelling: A

Effect of bombardment on anodizing

A crucial experiment is to determine if the supposed channelling is simply a result of the anodizing-stripping procedure being dose-sensitive. Thus large ranges could indicate merely a reduction in the amount of metal removed for a given anodizing voltage. Therefore, about 4×10^{16} ions/cm^2, corresponding to 100 μAmin/cm^2, were implanted in three Mo specimens at 10 keV; when these specimens were anodized at 40 volts and then stripped, it was found that the total amount of Mo removed was 48 μg/cm^2 as compared to 47.5 μg/cm^2 for similar but non-bombarded specimens (cf. equation 38). This suggests that the anodizing-stripping behaviour is not affected by implantation of energetic ions.

3.3.4 Evidence for Channelling: B

Crystallite Orientation

Since the Mo specimens used were polycrystalline in nature, it is obviously essential to determine the dominant crystallite orientations,

if any, of the specimens. Results of such an investigation for two specimens carried out on an X-ray diffractometer are summarized in Table IX.

We note from Table IX the striking result that <100>, <211> and <111> are virtually the only orientations; in the case of Mo, which has a b.c.c. structure, these are also the most open directions (i.e., least closed-packed). This large extent of openness of the structure may be one of the main reasons for the great discrepancy between the predicted and the observed ranges.

3.3.5 Evidence for Channelling: C

Dose Effect

We have argued above that when energetic ions are incident upon a crystalline target, they will partly undergo nuclear collisions and will partly get into channels and penetrate deep into the target. The initial incident ions have a greater probability of finding open channels since the target is initially devoid of any disorder; after these initial incident ions have undergone nuclear collisions, however, some of the target atoms will have been displaced and, therefore, any further incident ions will find this lattice disorder along their trajectory and should have a smaller probability of channelling. This effect was sought by carrying out the following two types of experiments.

In the first experiment, Mo targets were bombarded with radioactive Kr^{85} ions at 10 keV and at doses varying from 0.1 $\mu Amin/cm^2$ ($\sim 4 \times 10^{13}$ ions/cm^2) to 100 $\mu Amin/cm^2$ ($\sim 4 \times 10^{16}$ ions/cm^2). Comparisons of results from such experiments with theory can be made in two

TABLE IX

Radiation = Cu
Filter = Ni
λ = 1.5405 °A

d	hkl	2θ		I/I_1	Observed Peak Strength			
		expected	observed		Absolute x 10^2 i	ii	Normalized % i	ii
2.225	110	40.5	41	100	1.1	3.4	-	-
1.574	200	58.5	57-61.3	21	860	720	58.3	62.5
1.285	211	73.5	72.5-75.0	39	630	410	22.8	19.2
1.1137	220	87.4	89	11	-	-	-	-
0.9952	310	98.2	100	17	-	-	-	-
0.9085	222	115.2	114.5-117.0	7	93	70	18.9	18.3
0.8411	321	132.0	131.0	26	-	-	-	-

ways. The integral curves of Fig. 20 reveal significantly greater penetration than predicted from theory, though do not readily indicate the actual fraction of ions which so deeply penetrate. The differential curves of Fig. 21, obtained from the former by stepwise differentiation, permit a direct estimate of the extent of deep penetration. In fact, the total areas under the curves correspond to the total activity in the specimens. By subtracting the predicted profiles for amorphous targets from the observed profiles, the fraction of ions that are channelled, are deduced. It is seen that ∿90% of the ions are channelled at low doses and that this fraction reduces to ∿75% at higher doses, tentatively confirming the fact that the initial incident ions have a higher probability of channelling.

In the second experiment, one specimen was bombarded with 10 keV radioactive Kr^{85} ions (12.5 μAmin/cm^2) and the depth-distribution was determined. Then the same specimen was first prebombarded with inactive 10 keV Kr^{85} ions (12.5 μAmin/cm^2) so as to create defects in the structure along the path of the trajectory, and finally with radioactive 10 keV Kr^{85} ions (12.5 μAmin/cm^2). The results of these two experiments, expressed as integral concentration profiles, are shown in Fig. 22 and it is seen that prebombardment has moved the experimental curve towards the predicted Lindhard curve for amorphous targets. This further supports our initial postulate that the discrepancy between the experimental and the theoretical range profiles is due to crystal-lattice effects (channelling).

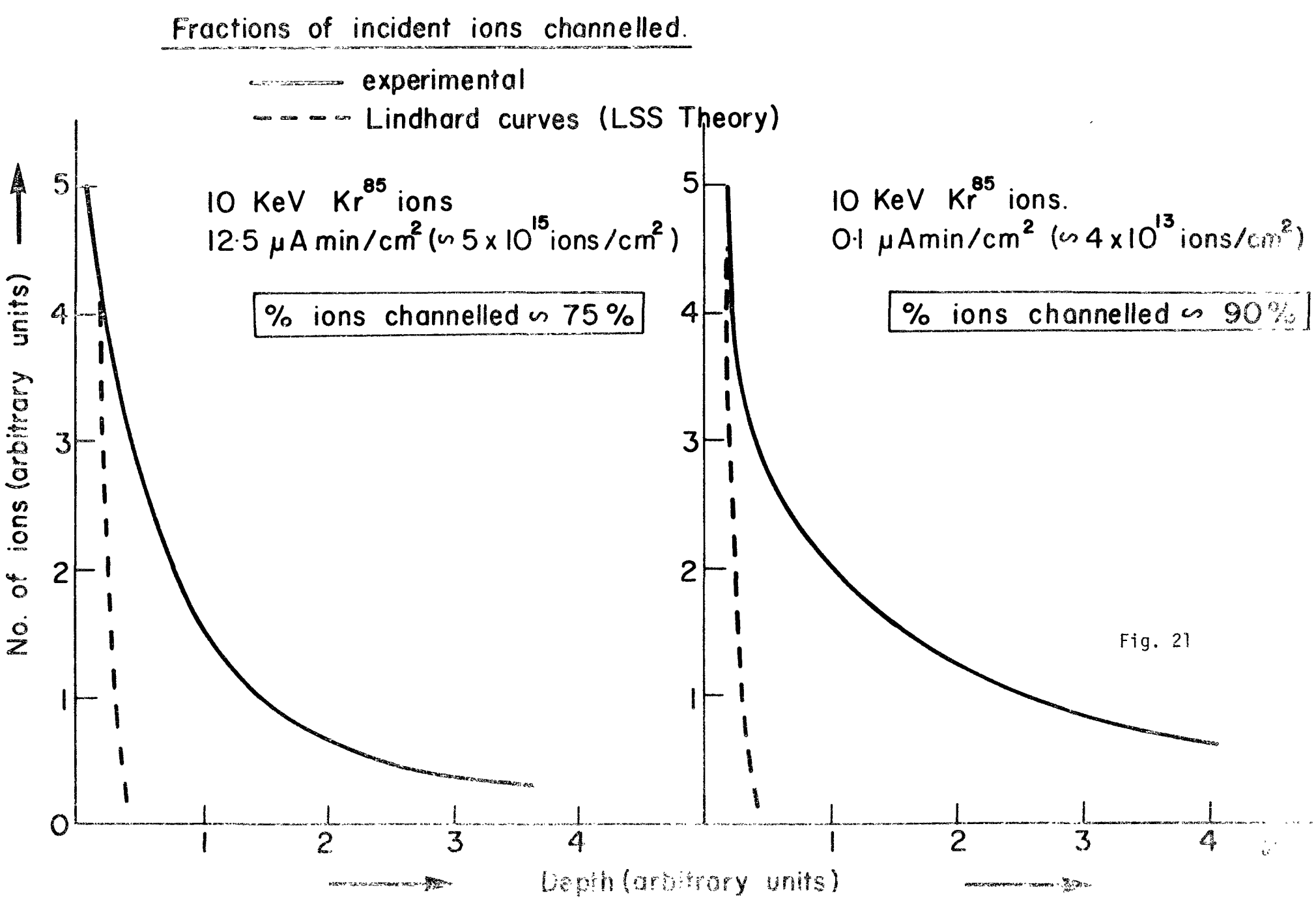
Fractions of incident ions channelled.
experimental
Lindhard curves (LSS Theory)
10 KeV Kr85 ions
12·5 μA min/cm2 (≃ 5 x 10^15 ions/cm2)
% ions channelled ≃ 75 %
10 KeV Kr85 ions.
0·1 μA min/cm2 (≃ 4 x 10^13 ions/cm2)
% ions channelled ≃ 90 %
No. of ions (arbitrary units)
Depth (arbitrary units)
0
1
2
3
4
5

Fig. 21

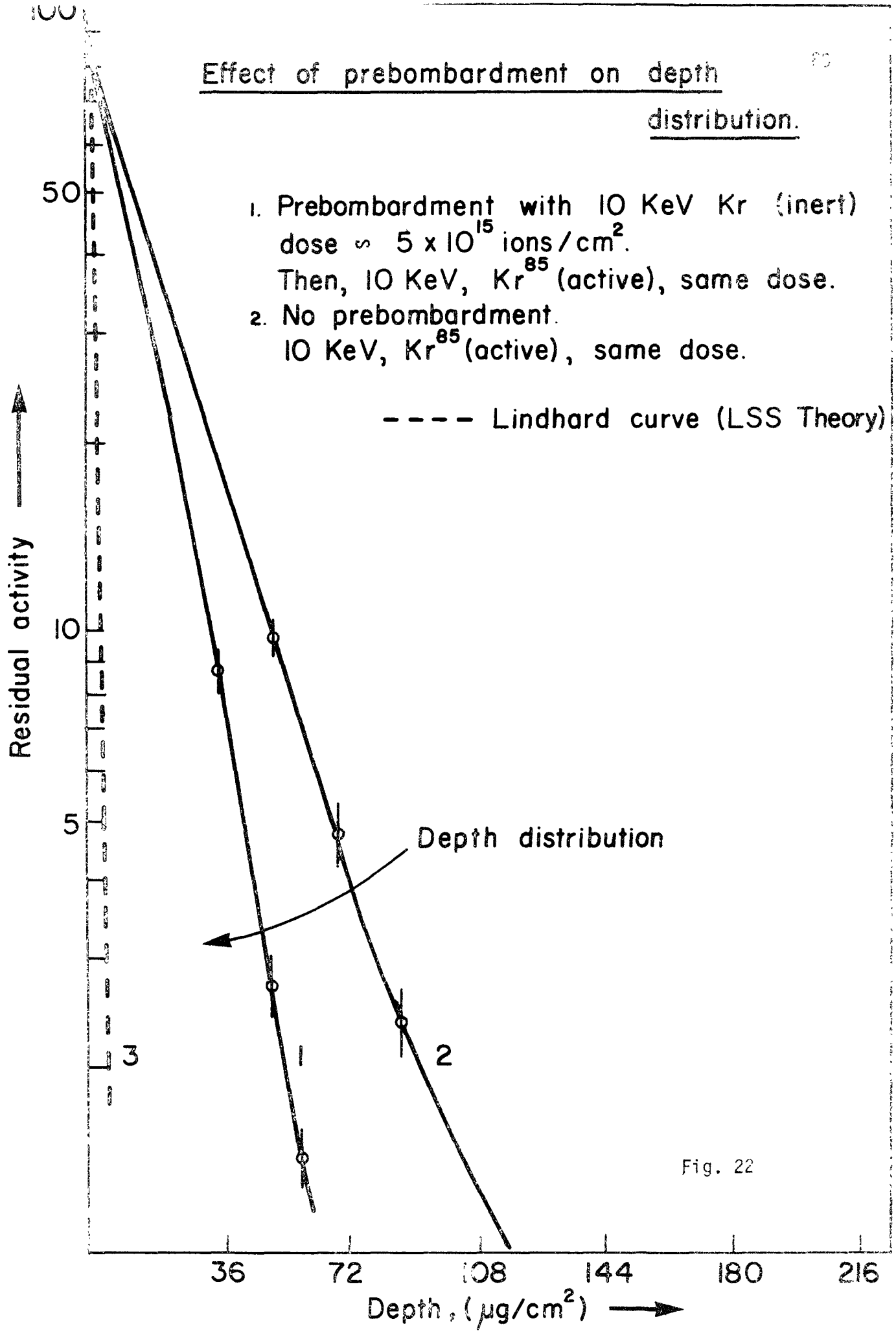
Effect of prebombardment on depth distribution.
1. Prebombardment with 10 KeV Kr (inert) dose ≈ 5 x 10^15 ions/cm^2.
Then, 10 KeV, Kr^85 (active), same dose.
2. No prebombardment.
10 KeV, Kr^85 (active), same dose.
---- Lindhard curve (LSS Theory)
Residual activity
100
50
10
5
3
Depth distribution
1
2
36
72
108
144
180
216
Depth, (μg/cm^2)

Fig. 22

CHAPTER 4

Summary and Future Work

The work described in this thesis may be summarized as follows:

(1) V and Mo have been, for the first time, successfully anodized under controlled conditions. W has been anodized to obtain a much thicker oxide film ($\sim$275 $\mu g/cm^2$) than was previously possible ($\sim$87 $\mu g/cm^2$).

(2) A technique has been developed and calibrated for removing thin uniform layers of known thicknesses from the surfaces of V and Mo. In essence, controlled anodizing, as in (1), is combined with dissolving the anodic oxides in 0.1 g/l KOH.

(3) The anodic films on Mo and W have been identified as being close in their composition to MoO_3 and WO_3. A similar definite conclusion was not possible with V, where compositions may range from $V_2O_{4.6}$ to V_2O_5.

(4) Depth distributions of energetic Kr^{85} in polycrystalline Mo were determined at various energies and doses. The results show that the ranges are much larger than those predicted by Lindhard's theory for amorphous targets. To confirm whether this discrepancy was due to crystal-lattice effects, i.e., channelling, additional experiments were carried out and their results are:

(a) High doses of ion-implantation do not affect the anodizing behaviour of Mo.

(b) The orientation of the specimens were mainly <100>, <211>

and <111>, these being also the directions most favourable to channelling.

(c) The fraction of ions channelled was ∿90% at low doses and ∿75% at a dose of 12.5 μAmin/cm^2.

(d) Prebombardment studies showed less penetration in specimens which had received preliminary bombardment with inactive Kr.

(5) Quantitatively, the results obtained are somewhat similar to those obtained for W by other workers. The significance of this is that the behaviour of W with regard to ion impact is well understood and may be extended to that of Mo.

Further investigations are required in the following areas:

(1) To deduce impact parameters, thence the critical angles for channelling, from the experimental results and to compare them with the values predicted from Lindhard theory.

(2) To extend this work to single crystals of Mo of known orientations. Such work will be in part done cooperatively with Dr. J.L. Whitton (Chalk River) in an effort to characterize $R_{max.}$.

(3) To study the depth-distributions of Kr^{85} in polycrystalline V and single crystals of V.

(4) To attempt to develop techniques for working with Be to truly complete the spectrum of accessible target masses.

REFERENCES

1. Nielsen, K.O., Electromagnetically enriched isotopes and mass-spectroscopy. Academic Press, Inc., New York; Butterworth & Co., London 1956. pp. 68 - 81.

2. Davies, J.A., Friesen, J., and McIntyre, J.D., Can. J. Chem. 38, 1526 (1960).

3. Whitton, J.L., and Davies, J.A., J. Electrochem. Soc. 111, 1347 (1964).

4. McCargo, M., Davies, J.A. and Brown, F., Can. J. Phys. 41, 1237 (1963).

5. Uhler, J., Domeij, B. and Borg, S., Arkiv för fysik, Band 24, nr. 30, 413 (1963).

6. Domeij, B., Brown, F., Davies, J.A., Piercy, G.R. and Kornelsen, E.V., Phys. Rev. Lett. 12 (13), 363 (1964).

7. Ericksson, L., Davies, J.A., Jespersgaard, P., Phys. Rev. 161 (2), 219 (1967).

8. Ericksson, L., Phys. Rev. 161 (2), 235 (1967).

9. Davies, J.A., Ericksson, L., Whitton, J.L., Can. J. Phys. 46, 573 (1968).

10. Kornelsen, E.V., Brown, F., Davies, J.A., Domeij, B. and Piercy, G.R., Phys. Rev. 136 (3A), A849 (1964)

11. Davies, J.A. and Jespersgaard, P., Can. J. Phys. 44, 1631 (1966)

12. Davies, J.A., Ball, G.C., Brown, F., and Domeij, B., Can. J. Phys. 42, 1070 (1964).

13. Dearnaley, G., Wilkins, M.A., Goode, P.D., Freeman, J.H., Gard, G.A., Harwell Publications C15 (1969).

14. Eisen, F.H., Can. J. Phys. 46, 561 (1968).

15. Piercy, G.R., McCargo, M., Brown, F. and Davies, J.A., Can. J. Phys. 42, 1116 (1964).

16. Domeij, B., Brown, F., Davies, J.A. and McCargo, M., Can. J. Phys. 42, 1624 (1964).

17. Davies, J.A., Domeij, B. and Uhler, J., Arkiv för Fysik, Band 24, nr. 27, 377 (1963).

18. Davies, J.A., Brown, F. and McCargo, M., Can. J. Phys. 41, 829 (1963).

19. Davies, J.A. and Sims, G.A., Can. J. Chem. 39, 601 (1961).

20. Jespersgaard, P. and Davies, J.A., Can. J. Phys. 45, 2938 (1967).

21. Bergström, I., Davies, J.A., Domeij, B. and Uhler, J., Arkiv. för Fysik. Band 24, nr. 28, 389 (1963).

22. Channing, D.A., Can. J. Phys. 45, 2455 (1967).

23. Verwey, E.J.W., Physica 2, 1059 (1935).

24. Mott, N.F., Trans. Faraday Soc. 43, 429 (1947).

25. Cabrera, N. and Mott, N.F., Repts. Prog. Physics 12, 163 (1948-9).

26. Young, L., Can. J. Chem. 37, 276 (1959).

27. Young, L., Anodic Oxide Films, Academic Press, London (1961).

28. Bean, C.P., Fisher, J.C. and Vermilyea, D.A., Phys. Rev. 105, 551 (1956).

29. Dewald, J.F., J. Phys. Chem. Solids 2, 55 (1957).

30. Young, L., Proc. Roy. Soc. A 258 496 (1960).

31. Vermilyea, D.A., Acta Met. 1, 282 (1953).

32. Vermilyea, D.A., J. Electrochem. Soc. 104, 427 (1957).

33. Young, L., Proc. Roy. Soc. A 263, 395 (1961).

34. Davies, J.A., Domeij, B., Pringle, J.P.S. and Brown, F., J. Electrochem. Soc. 112, 675 (1965).

35. Greenwood, N.N., Ionic Crystals, Lattice defects and Non-Stoichiometry, Butterworths, London (1968).

36. Wells, A.F., Structural Inorganic Chemistry, Third Ed., Oxford Press (1962).

37. Archer, R.J., Manual on Ellipsometry, Gaertner Scientific Corp., Chicago, U.S.A.

38. Archer, R.J., Shank, C.V., J. Opt. Soc. Amer. 57, 191 (1967).

39. Winterbottom, A.B., Optical Studies of Metal Surfaces, Kgl. Norske Videnskab. Selskab. skrifter Nr. 1, I. Kommisjon Hos. F. Bruns Bokhandel, Trondheim (1955).

40. Keil, R.G. and Salomon, R.E., J. Electrochem. Soc. 115, 628 (1968).

41. Aladjem, A., J. Mat. Science 3, 328 (1968).

42. Charlesby, A., Atomic Energy Research Establ. (Gt. Britain) Report M/R 714, 1951.

43. Lindhard, J., Scharff, M. and Schiøtt, H.E., Kgl. Danske Viedenskab. Selskab. Mat-Fys. Medd. 33, No. 14 (1963).

44. Winterbon, K.B., Sigmund, P. and Sanders, J.B., ibid. 37, No. 14 (1970).

45. Winterbon, K.B., Range-Energy Data for keV Ions in Amorphous Materials, AECL Rept. - 3194, Chalk River, Ont., Nov. 1968.

46. Sigmund, P. and Sanders, J.B., Conf. Appl. of Ion Beams Semi-Conductor Technology, Grenoble, May 24-26 (1967).

47. Moak, D.D., Reese, H., Jr. and Good, W.M., Nucleonics 9, 18, (1951).

48. Fetz, V.M. and Oechsner, H., Zeit Angew. Phys. 12, 250 (1960).

49. Pierce, J.R., Theory and Design of Electron Beams, Van Nostrand (1954).

50. Robinson, M.T. and Oen, O.S., Phys. Rev. 132, 2385 (1963).